Biphasic monolithic osteochondral scaffolds obtained by diffusion-limited enzymatic mineralization of gellan gum hydrogel

Abstract

Biphasic monolithic materials for the treatment of osteochondral defects were produced from polysaccharide hydrogel, gellan gum (GG). GG was enzymatically mineralized by alkaline phosphatase (ALP) in the presence of calcium glycerophosphate (CaGP). The desired distribution of the calcium phosphate (CaP) mineral phase was achieved by limiting the availability of CaGP to specific parts of the GG sample. Therefore, mineralization of GG was facilitated by the diffusion of CaGP, causing the formation of the CaP gradient. The distribution of CaP was analyzed along the cross section of the GG. The formation of a CaP gradient was mainly affected by the mineralization time and the ALP concentration. The formation of CaP was confirmed by Fourier transform infrared spectroscopy (FTIR), Raman spectroscopy and mapping, as well as energy-dispersive X-ray spectroscopy (EDX) mapping of the interphase. The microstructure of mineralized and non-mineralized parts of the material was characterized by scanning electron microscopy (SEM) and atomic force microscopy (AFM) showing sub-micrometer CaP crystal formation, resulting in increased surface roughness. Compression tests and rheometric analyzes showed a 10-fold increase in stiffness of the GG mineralized part. Concomitantly, micromechanical tests performed by AFM showed an increase of Young's modulus from 17.8 to more than 200 kPa. *In vitro* evaluation of biphasic scaffolds was performed in contact with osteoblast-like MG-63 cells. The mineralized parts of GG were preferentially colonized by the cells over the non-mineralized parts. The results showed that osteochondral scaffolds of the desired structure and properties can be made from GG using a diffusion-limited enzymatic mineralization method.

Keywords: biomaterials; tissue engineering; osteochondral; hydrogel; mineralization;

1. Introduction

Osteochondral defects involving structural damage to the articular cartilage and the underlying subchondral bone result in serious disability for millions of people worldwide [1,2]. For example, knee cartilage surgical techniques were performed in almost 36 thousand patients in the United States between 2007 and 2016 [3]. To date, all clinically accepted methods have been shown to have limited capacity to treat severe osteochondral lesions. Currently available techniques, such as debridement, mosaicplasty, microfracture, and implantation of autologous chondrocytes are considered short-term clinical solutions; therefore, the development of regenerative medicine and tissue engineering (TE) approaches is needed for both articular cartilage and subchondral bone [4,5].

Scaffolds for osteochondral regeneration are categorized into three types: monophasic, biphasic, and multiphasic. In monophasic scaffolds, the material is homogenous throughout the whole construct. Biphasic and multiphasic scaffolds are currently more popular approaches for providing the specific microenvironment for cartilage and bone regeneration. Commercially available scaffolds for osteochondral regenerations are: multiphasic MaioRegen® (Finceramica, Italy), biphasic TruFit® (Smith & Nephew, USA), biphasic Biomatrix™ CRD (Arthrex, USA), biphasic Agili-C™ (CartiHeal, Israel) [6]. There is still no clear consensus on the optimal scaffold design for osteochondral repair. The advantage of monophasic scaffolds is a relatively easy fabrication process. Experimental evidence indicates the superiority of biphasic and multiphasic designs over monophasic scaffolds, as they can mimic hierarchical structure of osteochondral tissue [7]. The most popular approach in research currently is the combination of two parts that mimic cartilage and bone regions [8–10].

The difference in composition and mechanical properties between bone and cartilage makes scaffold design and fabrication challenging. The compressive modulus of the subchondral bone ranges from 11 to 15 GPa [11]. The compressive modulus of the hyaline cartilage and the deep zones of the cartilage is 0.2-2 and 10 MPa, respectively [12,13]. The preparation of TE scaffolds should take into account different mechanical, physicochemical, and biological requirements for the material to regenerate cartilage and bone parts and preserve their integrity at the same time. The scaffold should act as an extracellular matrix (ECM) that provides spatial and temporal clues that promote individual growth of cartilage and bone tissues [14,15].

Over the years, many strategies have been investigated to create bilayer scaffolds for osteochondral application, but generally a mixture of several kinds of biomaterials with different additives is common in designing both layers. The cartilaginous layer is made of hydrogels based on natural or synthetic origin due to viscoelastic similarity to the native extracellular matrix (ECM), while

the lower subchondral layer is made of stronger materials such as bioceramics, metals, and harder polymers [16]. Many types of bilayer scaffolds have been investigated for osteochondral applications, containing different materials: natural polymers (collagen, glycosaminoglycans, chitosan, starch, hyaluronic acid, alginate, gellan gum), synthetic polymers (polylactide, polyglicolide, poly(lactide-co-glycolide), poly-ε-caprolactone), ceramics (hydroxyapatite, tricalcium phosphate, Bioglass®) and metals [5,17–19].

Integration between the chondral and bone layers in the osteochondral scaffold is of key importance. Poor integration may lead to delamination and final failure during tissue regeneration[20]. From this point of view, the best strategy is to produce a monolithic scaffold with tightly integrated parts made of the same or similar base material (only with different additives) or gradient material with gradually changing mechanical, chemical, and biological parameters [21].

Materials of recently increasing interest in biomedical applications are hydrogels [22–24]. Hydrogels are formed from three-dimensional physically or chemically cross-linked water binding networks [25]. The advantages of hydrogels include high similarity to natural ECM, good injectability, precise fitting to the defect site, and the feasibility of incorporation of bioactive molecules (e.g., growth factors) and cells, and finally good diffusion of nutrients and waste products [26,27]. Hydrogels have been considered mainly in soft tissue engineering, although their versatility has resulted in TE of their application in bone, cartilage [28–30] and for osteochondral applications [31–37].

Gellan gum (GG) is a calcium-cross-linkable polysaccharide hydrogel produced by bacteria (*Sphingomonas elodea*). GG has been applied in the food and pharmaceutical industries, as well as in controlled drug delivery. The advantages of GG are its low cost, high biocompatibility, biodegradability, and low toxicity of by-products and also the fact that it is not animal-derived, avoiding regulatory concerns [38]. More recently, GG has been considered a promising biomaterial for cartilage regeneration and treatment as injectable viscosupplement substituting hyaluronic acid [39–41]. The advantage of GG for cartilage tissue application is the structural similarity to the natural glycosaminoglycans (GAG) that make up cartilage. Regarding bone application, GG has recently gained interest due to its high affinity for calcium ions and its ability to be mineralized [39]. Mesenchymal stem cells inside the GG blends were recently printed using the extrusion method showing viability above 80% [42]. The osteochondral scaffold produced from GG and sodium alginate (for the chondral part) and GG with hydroxyapatite or magnesium phosphate (for the bone part) were used to regenerate rabbit osteochondral defects [34,36]. Printable bioink from GelMA-GG blends laden with primary chondrocytes supported chondrogenesis and deposition of cartilaginous matrix [43].

Mineralization with calcium phosphate (CaP) can be used to adapt hydrogels such as GG for bone regeneration purposes [44,45]. The osteoinductivity of different CaP biomaterials for bone regeneration was discussed in a review [46]. The most common way to obtain hydrogel with a mineral component is by adding ceramic powder to the hydrogel solution prior to gelation. The mineralization of the hydrogel can also be obtained by physical precipitation of insoluble phosphate within the hydrogel matrix – SBF [47] soaking or alternate soaking [48]. Another way to achieve mineralization of hydrogels is through enzymatic means [49,50].

GG was mineralized by incorporation of an enzyme, alkaline phosphatase (ALP) and incubation in solutions containing calcium ions and organic phosphate groups, e.g., calcium glycerophosphate (CaGP). ALP uses CaGP as a substrate, cleaving phosphate and thus increasing its local concentration, allowing precipitation of insoluble CaP [51]. The presence of mineral phase in a hydrogel matrix was found to improve bioactivity and biocompatibility with bone tissue, increased affinity for biologically active molecules (growth factors, interleukins), and modified mechanical properties [44,52,53]. Furthermore, the increase in roughness and stiffness caused by mineralization promoted cell differentiation toward the osteoblastic phenotype, providing a more appropriate environment for the formation of subchondral bone [54]. The physical and biological properties of enzymatically mineralized GG and other hydrogels for bone regeneration purposes studied by Douglas *et al*. resulted in a more than five-time increase in the storage modulus and a three-time increase in Young's modulus. The presence of CaP in mineralized samples promoted the attachment and vitality of osteoblastic MC3T3-E1 cells [44,51,55,56].

The purpose of this study was to produce a monolithic gradient or a bilayer scaffold for osteochondral applications using selective enzymatic mineralization of the GG hydrogel. We hypothesize that to develop a mineral gradient, the availability of a mineralizing substrate (i.e., CaGP) can be spatially limited to the specific sample surface. Therefore, by relaying on CaGP diffusion into the hydrogel, one part of the material supplied by CaGP should undergo mineralization, while the other part should remain unaltered. By this original approach, monolithic materials with gradually changing chemical composition, microstructure, and biological properties can be produced. The proposed method eliminates the need to combine two different materials and reduces the risk of delamination. The proposed method is also simple and low cost. We hypothesize that the biomimetic mineralization utilized in the process will lead to a more homogeneous distribution of the mineral phase and polymer-ceramic integration similar to that that naturally occurred in bone.

In particular, in this study, our objective is to: 1) investigate the usefulness of this innovative method to fabricate biphasic osteochondral scaffold, 2) find a correlation between the mineralization

parameters and the gradient profile of the mineral phase, 3) evaluate how the mineralization level affects the microstructure and mechanical properties of the resulting material, and 4) assess the biological response of model osteoblast-like cells cultured on biphasic materials.

2. Materials and methods

2.1. Materials

All materials, including 'low-acyl' GG (Gelzan™CM, G1910), ALP (P7640) and CaGP (50043) were obtained from Sigma-Aldrich, unless otherwise noted.

2.2. Hydrogel preparation

Hydrogels were prepared by heating GG solution to 90 °C and addition of $CaCl_2$ as a cross-linker. The final $CaCl_2$ concentration in the samples was 0.03% w/v. After cooling to 60 °C, an aqueous solution of ALP was added to the final concentration of 2.5 mg/ml. Gel casting was performed immediately after ALP addition to minimize loss of ALP activity. It was also demonstrated (Appendix: Supplementary Figure) that ALP retains more than 90% activity at 60 °C for 30 min, but quickly loses its activity at temperatures higher than 65 °C. The gel preparation at a temperature higher than 50 °C (proposed by Douglas [55]) allowed more concentrated GG hydrogels to be produced.

The biphasic hydrogel samples were prepared as described above; however, the hydrogel was casted into the wells of a 24-well plate and covered with glass slides providing a flat surface without meniscus. After gelation, glass slides were removed. For AFM experiments, gel solution was casted into polyethylene (PE) ring (f = 10 mm, h = 1 mm) glued to glass slide (bottom part of the liquid cell of the AFM apparatus) and then covered with glass cover-slip providing flat top surface. The samples were then left for 30 min at 4 °C for gelation. Subsequently, the glass coverslip was gently removed. For FTIR, SEM, mechanical and rheology tests the samples were casted into Petri dish and after gelation cylinders of 12 or 25 mm in diameter and 4 and 2 mm in height, respectively, were cut.

2.3. Mineralization

GG samples were enzymatically mineralized using ALP and CaGP as a substrate. ALP increases mineral deposition by cleavage of the phosphate group from organic phosphate, thereby increasing the local phosphate concentration and enabling precipitation of the CaP phase inside the material. Calcium and glycerophosphate ions diffuse into the hydrogel matrix containing ALP. Cleaved

phosphate ions react with calcium ions to form insoluble CaP, which remains trapped within the gel. The by-product glycerol is released into the surrounding environment (Fig. 1(a)).

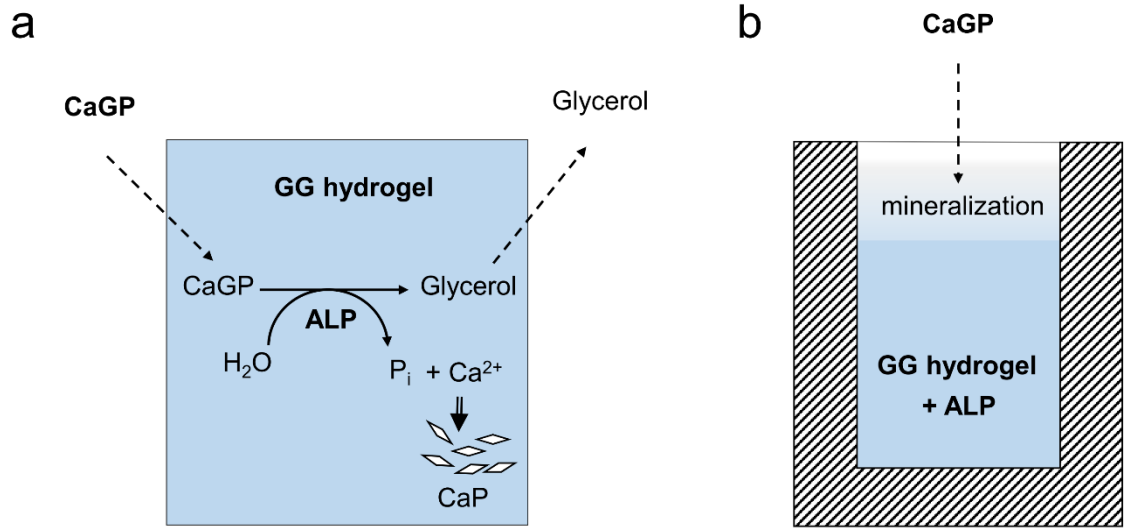

Fig. 1 Bulk enzymatic mineralization of GG hydrogel by ALP and CaGP (a) and diffusion-limited enzymatic mineralization used to obtain biphasic osteochondral scaffolds (b).

The samples were incubated in 0.1 M CaGP (prepared by dissolving CaGP powder in ddH_2O followed by 30 min of ultrasonication) at room temperature for 1 and 72 h. For micromechanical tests and surface topography by AFM, the mineralization was carried out by submerging the glass slides with PE rings containing a hydrogel in 0.1 M CaGP. The CaGP solution was changed every day. After mineralization, the samples were rinsed and subsequently incubated in ddH_2O for 1 day to remove residual CaGP. Nonmineralized hydrogels were used as controls.

Biphasic monolithic scaffold were obtained by exposing only the top part of cylindrical samples casted into a 24-well cell culture plate to CaGP mineralizing solution (Fig. 1(b)). The samples were partially mineralized because of the limitation of CaGP diffusion to deeper parts of the material caused by mineral formation. A GG hydrogel of different concentrations (0.7, 1.0 and 1.3%) and ALP content (0.1 – 5.0 mg/ml) were prepared. The samples were mineralized for 24, 72 and 168 h.

2.4. Determination of CaP content

To determine dry mass, which is a parameter that describes CaP content within hydrogels, the samples were weighted, dried for 48 h, and again weighted. The dry mass percentage was calculated as follows:

$$\text{Dry mass } (\%) = \frac{\text{weight after incubation and drying}}{\text{weight after incubation before drying}} * 100\%$$

The content of CaP was calculated by subtracting the theoretical dry mass % of GG (that is, 0.7%, 1%, 1.3%) from the dry mass (%) for each sample. For each type of material, 4 samples were tested. To determine the CaP profile along the direction of mineralization gradient, series of round slices (0.8 mm thick) were cut from cylindrical samples. The CaP content for each slice was determined as described before.

2.5. Scanning electron microscopy (SEM) and energy dispersive X-ray (EDX) spectroscopy

SEM analysis was performed on a TM3030 tabletop microscope (Hitachi, Tokyo, Japan) with EDX analyzer (Bruker Quantax 70, Billerica, Massachusetts, United States). Before SEM analysis, the samples were freeze dried for 24 h, attached to the holder by carbon sticky tape, and coated with a thin gold layer (Cressington 108 Sputter Coater, Watford, UK). In the case of EDX analysis, samples were studied without coating. Images were collected at a 15 kV acceleration voltage. To obtain high-resolution SEM images backscatter electron detector (BSD) mode in Gemini SEM 500 (Zeiss, Jena, Germany) was used.

2.6. Fourier transform infrared (FTIR) spectroscopy and Raman spectroscopy

After mineralization and drying (37 °C, 48 h), the molecular structure of the samples was examined by ATR-FTIR attenuated total reflectance. FTIR transmittance spectra were acquired using a Tensor 27 spectrometer (Bruker) equipped with standard Pike ATR cell and diamond ATR crystal. Spectra were recorded over the range 4000–525 cm^{-1} at a resolution of 4 cm^{-1} for 64 accumulations.

For Raman spectroscopy and mapping the samples were prepared as a thin (< 1 mm) slice, dried (37 °C, 48 h) and attached to the glass slide with two-sided sticky tape (carbon tape). Raman spectra for mineralized and non-mineralized parts of the sample were recorded using RISE Raman microscopy (WITec, Ulm, Germany). Raman maps were obtained by collecting spectra from 500 µm x 200 µm fragment and 20 μm^2 resolution. Data were processed using Project FOUR 4.1 software to obtain a distribution map for phosphate corresponding to the band at 963 cm^{-1}.

2.7. Mechanical properties

Mineralized hydrogels (samples 12 mm in diameter and 4 mm in height) were subjected to compression testing using ZWICK 1435 (Zwick Roell, Ulm, Germany). Hydrogels were placed between

piston heads and displacement was applied at a rate of 1 mm/min until the samples were compressed to 10% of their original height. Young's modulus (E) was determined on the stress-strain curve. For each sample group, 4 samples were tested.

Rheological measurements were made on an MCR 301 rheometer (Anton Paar, Graz, Austria) in parallel plate geometry equipped with a PP25 rotating head of diameter 25 mm. Samples 25 mm in diameter and 1 mm in height were tested in triplicate. Storage modulus (G') and loss modulus (G'') values were recorded at a frequency of 1.0 Hz and 0.1% strain.

2.8. Atomic force microscopy (AFM) imaging

Experiments were performed on dried hydrogels as well as hydrated hydrogels surrounded by deionized water (Millipore) on an MFP-3D atomic force microscope (Asylum Research, Oxford Instruments Company, Santa Barbara, CA) in liquid cell (Portless Fluid Dish Accessory for the MFP-3D™ AFM) with the use of an AC240TS cantilever at 21^{o}C.

Dry samples were imaged in dynamic force mode (AC mode) and contact mode. Three sample types were studied: unmodified 0.7% GG gel, 0.7% GG gel containing 2.5 mg/ml ALP mineralized for 1 h and 0.7% GG gel containing 2.5 mg/ml ALP mineralized for 72 h. Flat films of dried gels were attached to glass slide by sticky tape. Each cantilever was calibrated in air with Get REAL in Igor 15.0 software. The calibration protocol measured the thermal noise spectrum and on the basis of the Sader method, the spring constant and invOLS were acquired. The images were collected with low scanning rate (0.2 Hz) and low setpoint (20-70 mV).

Hydratated hydrogel was imaged in AC mode, covered by deionized water in the liquid cell. A thin layer of 0.7% GG gel containing 2.5 mg/ml ALP was placed on a bottom liquid cell glass and kept in CaGP solution for 3 days. Subsequently, the gel was washed in deionized water and subsequently incubated in deionized water for 1 day. The spring constant and the resonant frequency were determined by thermal tuning. AC-mode AFM images were collected from flat parts of the surface. The sample was scanned with the PNP-TR cantilever. The driving amplitude for this scan was 300 mV with a setpoint of 25 mV. Higher oscillation amplitudes prevented the cantilever tip from sticking to the gel during slow scanning. However, higher amplitudes (above 500 mV) blurred the image due to sample perturbation by oscillating tip. Scans were collected with a low scanning rate (0.1 Hz) to minimize perturbation.

Images were saved in original non-flattened format and subsequently processed by Gwyddion software (flattening, lines correction).

2.9. Micromechanical properties

Force-distance curves of material with different levels of mineralization, as well as non-mineralized GG gel in water were obtained with an Asylum Research, MFP-3 atomic force microscope. Force curves were collected in contact mode with the AC240TS cantilever (Olympus, spring constant: 0.3 - 4.8 N/m). 40 x 40 points maps of nanoindentation curves were collected from a square area of 50 µm x 50 µm.

The maximum force applied onto the hydrogel surface in the elastic indentation was 15 nN for AC240TS-R3 cantilevers, which corresponded to 100 mV trigger point. In order to convert the cantilever deflection signal from millivolts (mV) to nm (force-indentation), the deflection sensitivity of the instrument, and so the sensitivity of the probe, was calculated from calibration measurements on mica substrate, assumed to be an infinitely rigid substrate (zero indentation). The spring constant and the resonant frequency were determined by thermal tuning according to the spring constant tutor in Igor 15.0 software. The elastic modulus (E) for all the collected maps was determined by fitting a Hertz mathematical model. For all measurements v was assumed to be 0.5 [57].

2.10. Biological tests

Biphasic hydrogel slices obtained by cross section along to gradient direction were incubated in 24-well plates (Nunclon) at 37°C for 2 h in Dulbecco's Modified Eagle Medium (DMEM PAA, Austria) supplemented with 10% fetal bovine serum, 1% penicilin/streptomicin, 2 mM L-glutamine (PAA, Austria). 200 µl of osteoblast-like MG-63 cells (European Collection of Cell Cultures, Salisbury, UK) were seeded on each sample ($3x10^4$ cells) and allowed to sediment. After 10 min, 800 µl of medium was added and cultures were carried out for 4 and 8 days at 37 °C and 5% CO_2.

Cell viability and morphology were evaluated after 4 and 8 days of incubation using live/dead staining and fluorescence microscopy. Cell culture medium was removed from each well and replaced with 1 ml of the staining solution – 0.1% calcein AM and 0.1% propidium iodide (Sigma) in PBS. Cells were incubated in the dark for 20 min at room temperature. Fluorescence microscopy images were taken using an Axiovert 40 CFL with HXP 120 C metal halide illuminator (Zeiss, Germany).

The metabolic activity of the cells was tested using an MTS assay (CellTiter 96® Aqueous One Solution Cell Proliferation Assay, Promega). 4 samples for each of 2 groups were tested – one mineralized for 3 days and the second non-mineralized. The hydrogels were prepared as previously described and seeded with $8x10^4$ cells on each sample. Cells were cultured for 4 and 8 days in DMEM (supplemented with 10% foetal bovine serum, 1% penicilin/streptomicin, 2mM L-glutamine), at 37 °C

and 5% CO_2. The MTS test was performed after the samples to fresh plates. 500 μl of DMEM was added for each sample followed by the addition of 100 μl MTS reagent. Cells were incubated for 4 h at 37°C and 5% CO_2. The concentration of soluble formazan was measured by FLUOstar Omega Microplate Reader (BMG LABTECH) at 570 nm. The results were presented as averages of 4 samples with standard deviations. Statistical analysis was performed according to the ANOVA test combined with a post hoc Tukey-Kramer multiple comparisons test at $p<0.001$.

3. Results

3.1. Morphology

To obtain biphasic monolithic samples, the mineralization of GG was carried out in a way in which CaGP substrate was provided from the upper surface of a cylindrical hydrogel. The level of mineralization, measured by the percentage of dry mass, gradually increased over time for all samples (Fig. 2). The material was mineralized only from the side that was in contact with the CaGP substrate. The opposite side remained non-mineralized for all samples, with some small exceptions, little globular precipitates or flat, thin layers in a non-mineralized zone. Usually, the mineralized zone that was produced during the first day of mineralization was not progressing deeper into the hydrogel. Only the level of mineralization was increasing. This way of mineralization in every case produced a sharp transition between mineralized and non-mineralized zones. Most of the mineralization took place in the bulk of the hydrogel with few exceptions.

In the experiments, two different parameters of the hydrogel were tested: ALP concentration (from 0.1 to 5 mg/ml) and GG concentration (from 0.7 to 1.3%) (Fig. 2). The first had a much more substantial effect on the mineralization process and CaP formation. For the lowest ALP concentration (Fig. 2 (g), (h), (i)), mineralization was slower, the maximum level of mineralization was lower, but the mineralized zone was deeper (approximately 8 mm depth). The samples with the highest percentage of ALP (Fig. 2 (a),(b),(c)) were mineralized very strongly close to the top surface and the mineralization zone did not penetrate more than 2 mm into the material. For these samples, the level of CaP mineralization after 7 days was around 20%.

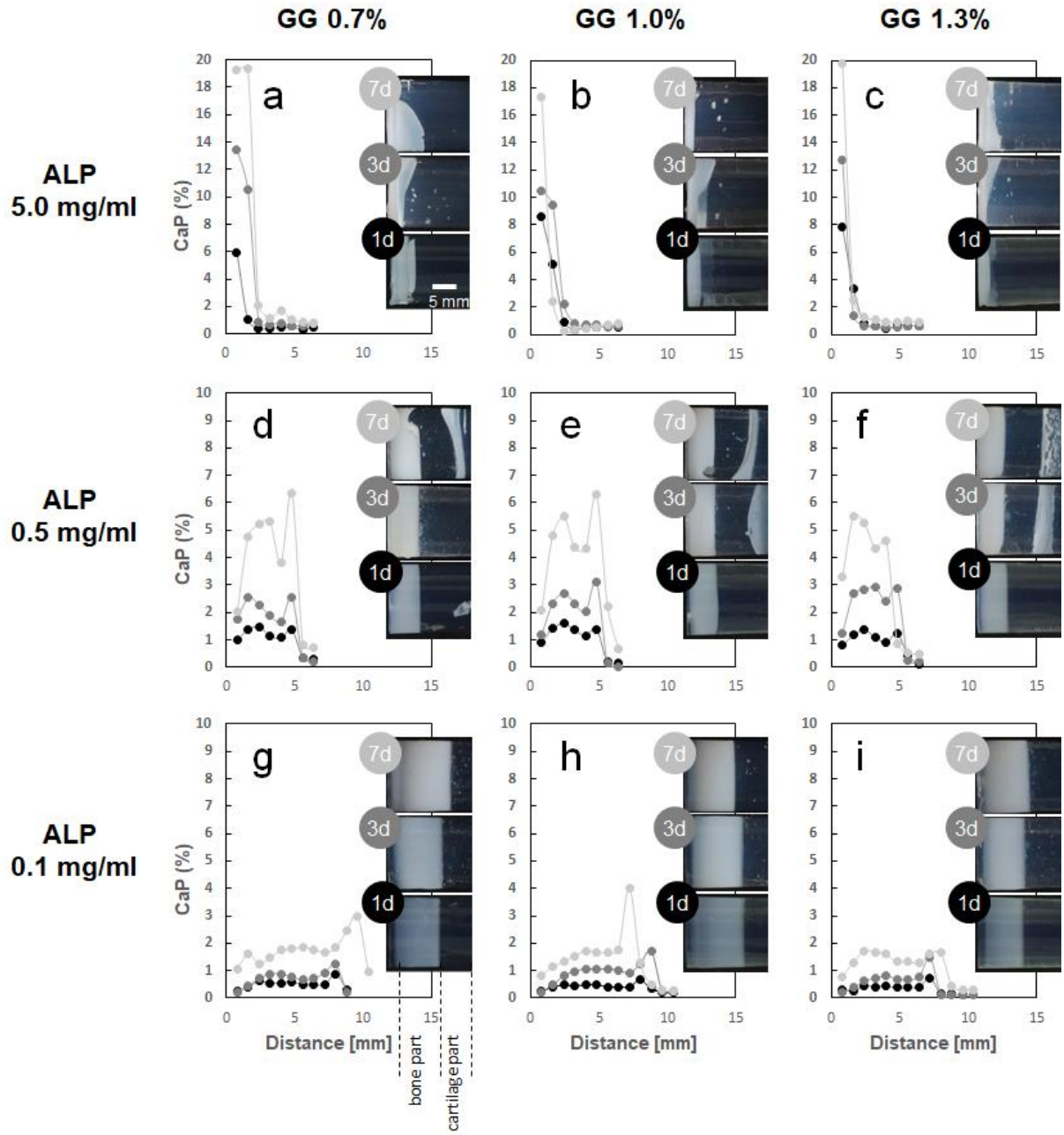

Fig. 2 CaP percentage profiles (left side) of biphasic GG hydrogels mineralized over 1 day (•, 1d), 3 days (•, 3d) and 7 days (•, 7d) and morphology of gradient samples used to create mineralization profile (right side). Left part of each picture shows white mineralized bone part, while left part shows transparent non-mineralized cartilage part as marked in (g). Three different concentrations of ALP were used: 5.0 mg/ml (a), (b), (c), 0.5 mg/ml (d), (e), (f) and 0.1 mg/ml (g), (h), (i). Three concentration of GG were used: 0.7% (a), (d), (g), 1.0% (b), (e), (h) and 1.3% (c), (f), (i). Scale bar marked in (a) equal to 5 mm is valid for all the pictures (a)-(i).

The intermediate level of mineralization (Fig. 2 (d),(e),(f)) was for ALP 0.5 mg/ml samples (around 5% after 7 days) and also the mineralization zone depth was between that noted for samples with 0.1 and 5 mg/ml ALP (5 mm depth). Samples with the lowest ALP concentration had the most uniform and homogeneous profile of mineralization: the interphase between two zones was straight, there was no mineralization outside, and no mineralization inside the non-mineralized zone. For 0.5 mg/ml ALP (Fig. 2 (d), (e), (f)) the mineralization profile was less uniform and thin mineralized surfaces

were present inside the non-mineralized zone after a longer mineralization time. However, in this case, no mineral deposits were present on the side surface of the hydrogel, which was the case for the 5 mg/ml ALP hydrogel (Fig. 2 (a),(b),(c)). For those samples, small mineralized globules were also present inside the non-mineralized zone. Part of a material closer to the top surface (between 0 and 2 mm) was poorly mineralized in the case of 0.5 and 0.1 mg/ml ALP samples (Fig. 2 (d)-(i)) and very strongly mineralized for 5 mg/ml ALP samples (Fig. 2 (a), (b), (c)).

The highest level of mineralization was reached close to the gel surface for 5 mg/ml ALP samples (Fig. 2 (a)-(c)) and close to the interface for 0.5 and 0.1 mg/ml ALP samples (Fig. 2 (d)-(i)). For the 0.1 mg/ml ALP sample, this phenomenon of an increased level of mineralization at the interface was much stronger than for the 0.5 mg/ml ALP sample and in some cases was twice that of the rest of the mineralized zone. Interestingly, this phenomenon was not present (or only to a small degree) in 1.3% GG samples (Fig. 2 (i)).

Differences between various concentrations of GG were mostly visible for GG containing 0.1 mg/ml ALP. In this case, there was a slight progression of the mineralization zone into the hydrogel over time for 0.7 and 1.3% GG and the opposite effect was observed for 1.0% GG. The second difference related to GG concentrations is the much higher level of mineralization at the interface for 0.7% and 1.0% GG, which was not that prominent for the 1.3% GG samples (Fig. 2 (f), (i)).

3.2. Chemical analysis

SEM and EDX analysis of the mineralized sample (0.7% GG + 0.5 mg/ml ALP) for 72 h revealed the presence of calcium and phosphorus in the mineralized part and only a small amount of these elements in the other part (Fig. 3 (b)-(d)). In the mineralized part there was a much higher signal from Ca and P than from carbon or oxygen. The Ca/P ratio for the mineralized part was close to 1.0. The EDX maps revealed a sharp transition between mineralized and non-mineralized zones in terms of Ca and P. The same sharp transition was recorded in Raman spectroscopy mapping (Fig. 4 (d)) corresponding to 963 cm^{-1} peak related to symmetric ν_1 PO_4^{3-} stretching in phosphate group. Another Raman shift at 1072 cm^{-1} (ν_3 asymmetric stretch) peak characteristic for crystalline hydroxyapatite was present, although it had a very small intensity. The presence of phosphate groups was also confirmed by FTIR spectroscopy for the mineralized part of the sample (Fig. 4 (f)). Peaks at 557 and 598 cm^{-1} were attributed to ν_4 vibration components of PO_4^{3-}. Peaks between 970-1100 cm^{-1} were attributed to the ν_1 and ν_3 stretching of PO_4^{3-} groups. These bands overlapped with the 1020 cm^{-1} band (Fig. 4 (e)) related to the stretching C-O vibration of GG [58].

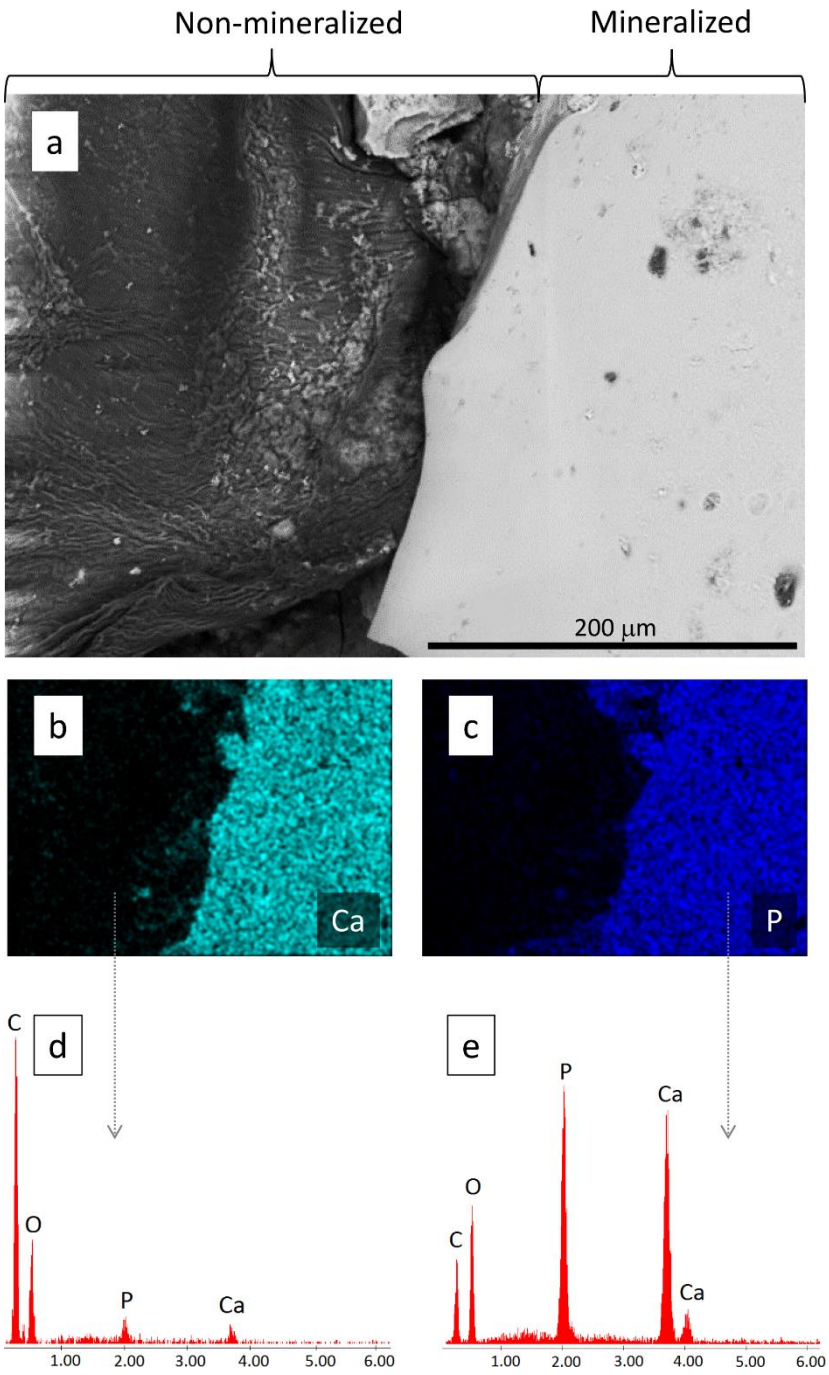

Fig. 3 SEM image of interface between mineralized (right) and non-mineralized (left) phase of biphasic GG sample (a), corresponding EDX maps of calcium (b) and phosphorus (c) and respective EDX spectra of calcium (d) and phosphorus (e). All samples after diffusion-limited mineralization in CaGP for 72 h.

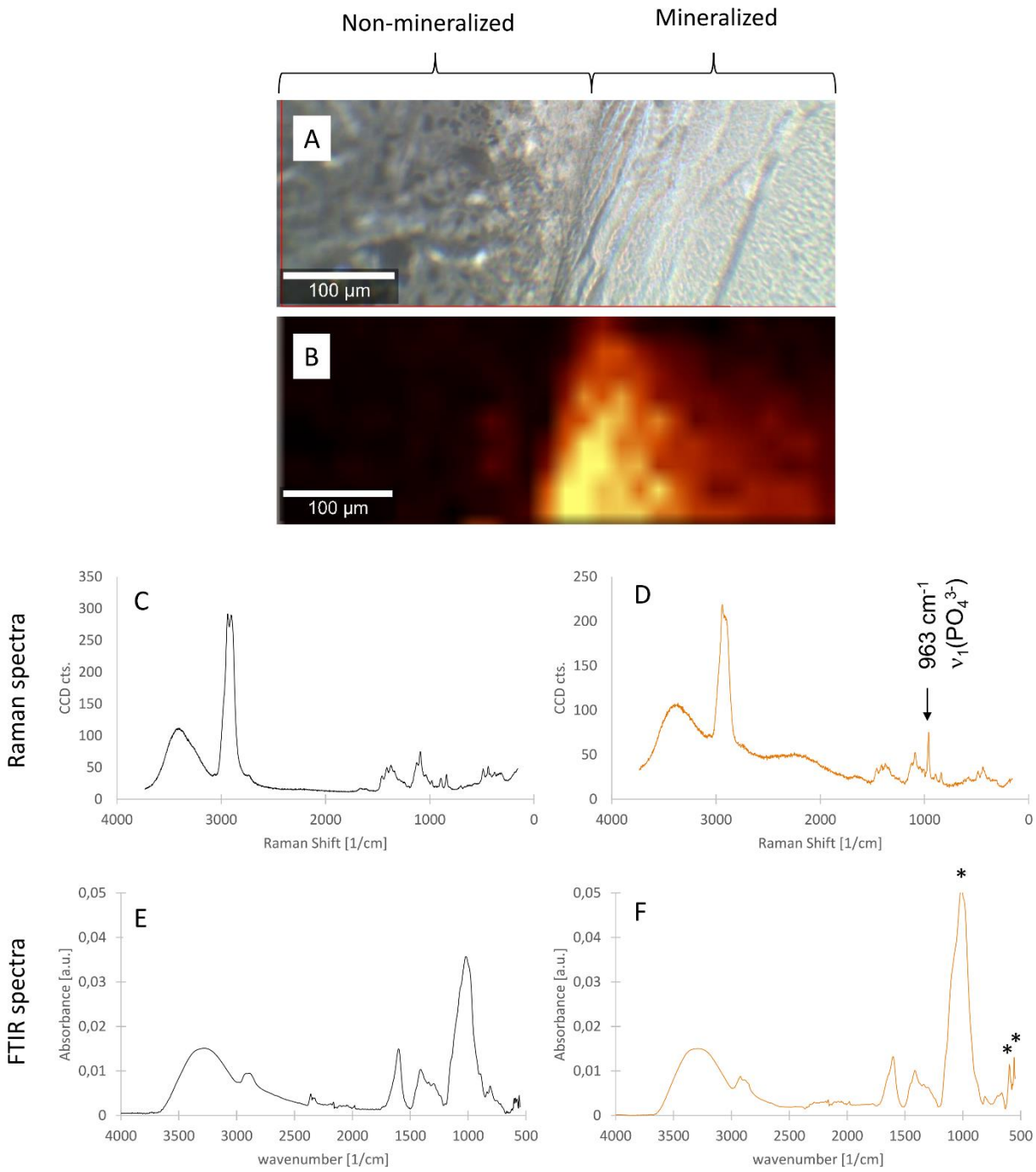

Fig. 4 Interface between mineralized (right) and non-mineralized (left) phase of biphasic GG sample (a, b). Confocal microscope image (a) and corresponding Raman map for the band at 963 cm^{-1} (b). Raman spectra of non-mineralized (c) and mineralized part (d) of GG biphasic sample. FTIR spectra of non-mineralized (e) and mineralized (g) part of GG biphasic sample. All samples after diffusion-limited mineralization in CaGP for 72 h.

3.3. Microstructure

The freeze dried non-mineralized GG was smooth (Fig. 5 (a)), while those mineralized for 72 h in CaGP showed mineral deposits that formed small globules with pores between them (Fig. 5 (b)). The white colour in the SEM image in BSD mode shows the presence of elements with higher atomic mass, such as calcium and potassium. The distribution of mineral deposits was not uniform. There were places with a more condensed and looser structure.

AFM images collected in the wet state under water showed a smooth surface for the non-mineralized sample (Fig. 5 (c)) and the presence of globules and pores in the mineralized sample (Fig. 5 (d)). Mineralized GG was rough (Ra = 33.6 $\pm$ 2.7 nm, RMS = 349 $\pm$ 22 nm) as compared to more wavy and smooth non-mineralized GG (Ra = 3.9 $\pm$ 1.1 nm, RMS = 141 $\pm$ 61 nm). The size of the globules was estimated to be around 500 nm. Higher magnification AFM images of GG samples in a dried state after mineralization (Fig. 5 (f)) showed the internal structure of globules made of even smaller features, probably mineral nanocrystals visible as small dots, 10-20 nm in diameter. The non-mineralized GG after drying looked similar, it was also rough but much more uniform and without nanocrystals visible (Fig. 5 (e)).

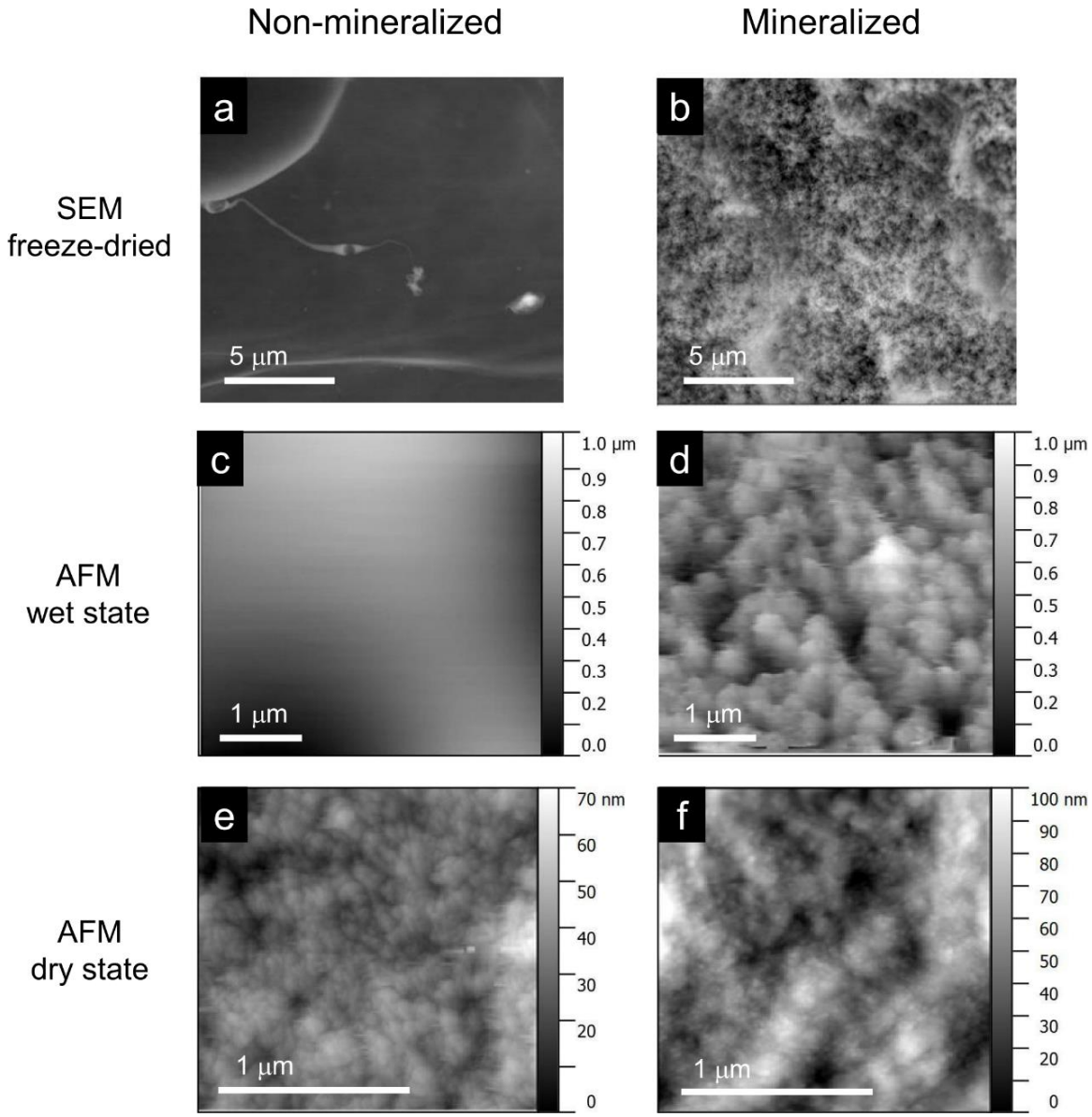

Fig. 5 SEM images in BSD mode (a, b) and AFM (c, d, e, f) images of GG microstructure: non-mineralized (a, c, e) and after 72 h mineralization in CaGP (b, d, f). AFM on samples in water (c, d) and in dry state (e, f).

3.4. Mechanical properties

The mechanical properties of mineralized and non-mineralized GG studied by AFM, compression test, and rheology are shown in Fig. 6. The stiffness map for non-mineralized GG (Fig. 6 (a)) was uniform with only low Young's modulus values (median 17.8 kPa). The stiffness map for mineralized GG (Fig. 5 (b)) was less uniform with places with a high (500 kPa) Young's modulus and places with a low (<20 kPa) E value that formed holes between the more rigid regions. The distribution of E values (Fig. 6 (c),(d)) was very narrow for non-mineralized GG and spread to higher values after mineralization, achieving a median value of 206.5 kPa.

The bulk stiffness measurement of 0.7% GG containing 0.5 mg/ml ALP in compressive test showed a 20-fold increase in the E modules after 72 h of mineralization. The storage modulus (G') increased an order of magnitude during mineralization and the loss modulus (G'') increased more than two orders of magnitude (Fig. 6 (e), (f)).

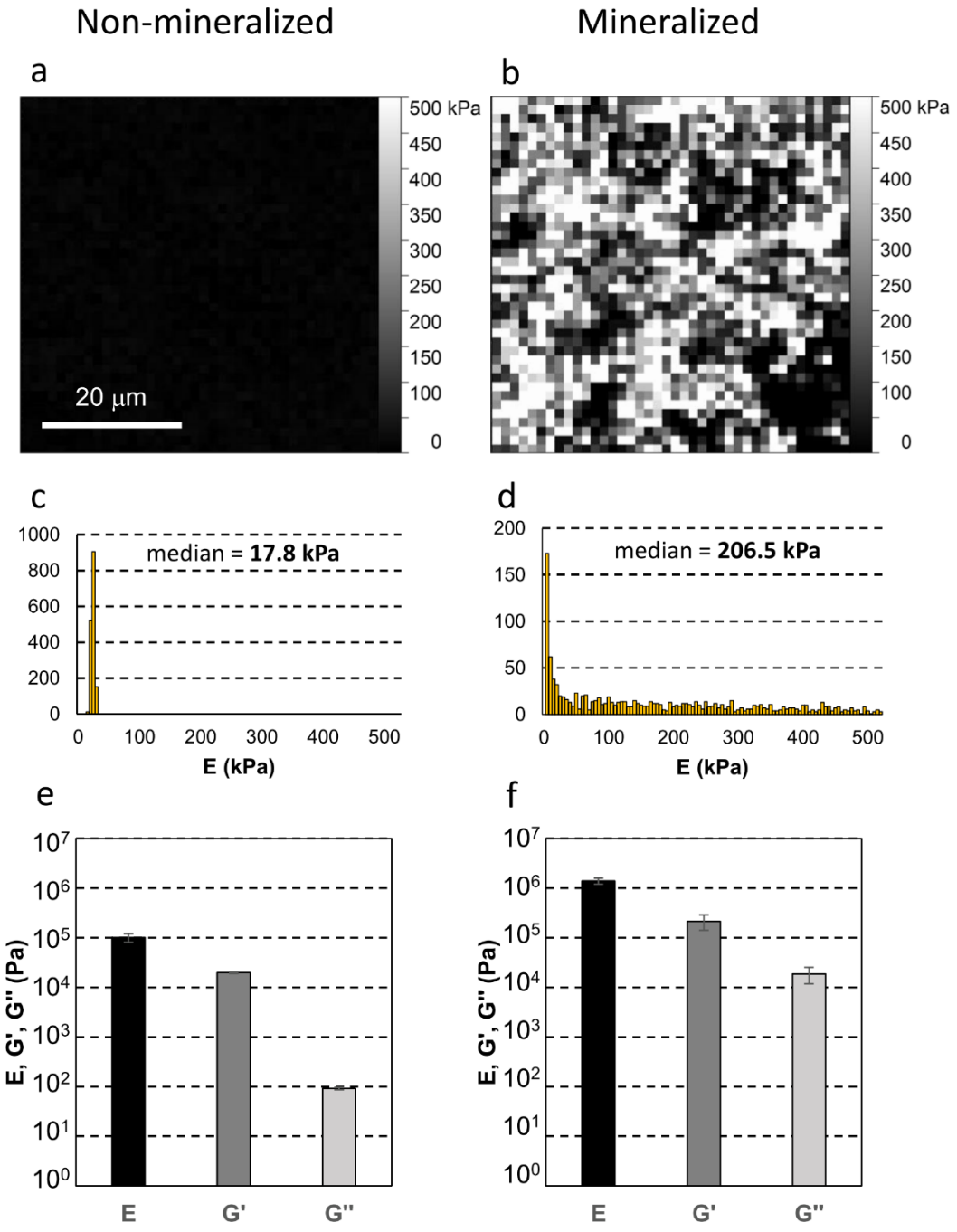

Fig. 6 Young's modulus maps for 0.7% GG containing 0.5 mg/ml ALP before (a) and after mineralization (b) in aqueous environment measured by AFM (a, b) and corresponding Young's modulus distribution diagrams (c, d). Bulk Young's modulus studied by Zwick, storage (G') and loss modulus (G'') studied by rheology before (e) and after 72 h mineralization (f). Error bars show standard deviation.

3.5. Biological response

The behaviour of MG-63 cells on non-mineralized, mineralized, and biphasic GG samples is shown in Fig. 7. After 8 days of culture, cells were grown on non-mineralized GG in the form of agglomerates. Cells were mostly round, poorly spread, and their number was low (Fig. 7 (a)). On mineralized material (Fig. 7 (b)) almost the entire surface was covered by cells. Live/dead staining showed very little number of dead cells on both materials (less than 2%). Cell viability, as studied by the MTS test, was almost ten times higher on mineralized samples than on non-mineralized samples (Fig. 7 (c)). Cells on mineralized GG had higher viability than those cultured on non-mineralized GG. Cell viability on non-mineralized material increased between day 4 and day 8, however, there was no increase in viability for cells growing on mineralized GG in the same period of time.

MG-63 cells were also cultured in 0.7% GG subjected to gradient mineralization for 8 days (Fig. 7 (d), (e)). Almost all cells were growing on the mineralized side, they were well spread and elongated, with morphology compared to that on the mineralized sample (Fig. 7 (b)). The non-mineralized part remained almost completely empty except for one small cell agglomerate close to the interface non-mineralized/mineralized zone.

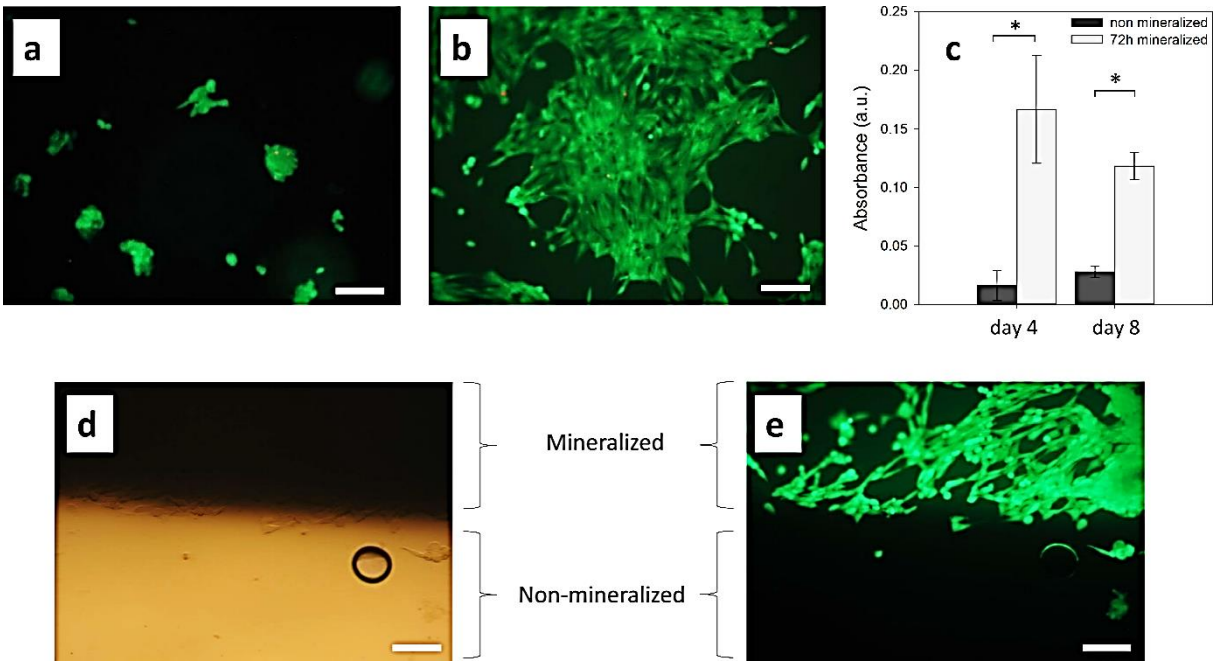

Fig. 7 Fluorescent images after live/dead staining of MG-63 cells cultured on 0.7% GG (a) and mineralized 0.7% GG for 8 days (b). MTS test for cells cultured on those materials (c), *$p < 0.001$, error bars show standard deviation. Morphology of MG-63 cells cultured at the interface non-mineralized/mineralized zone (d, e); optical microphotography (d), fluorescent microscopy after live/dead staining (e), white bar = 100 μm.

4. Discussion

4.1. Mineralization profile

The primary objective of this research was to develop a method that can selectively alter one part of the hydrogel material by producing a mineral content and stiffness that is considered favourable in regeneration of osteochondral region regeneration as it can closely resemble naturally occurring gradients [15]. Because of the diffusion-limited enzymatic mineralization method developed in this study, it was possible to produce a biphasic monolithic hydrogel scaffold in which only one part was mineralized, while the other remained unaltered. The mineralization profile was not influenced by the concentration of GG, but was mainly dependent on the concentration of ALP and the duration of the mineralization process.

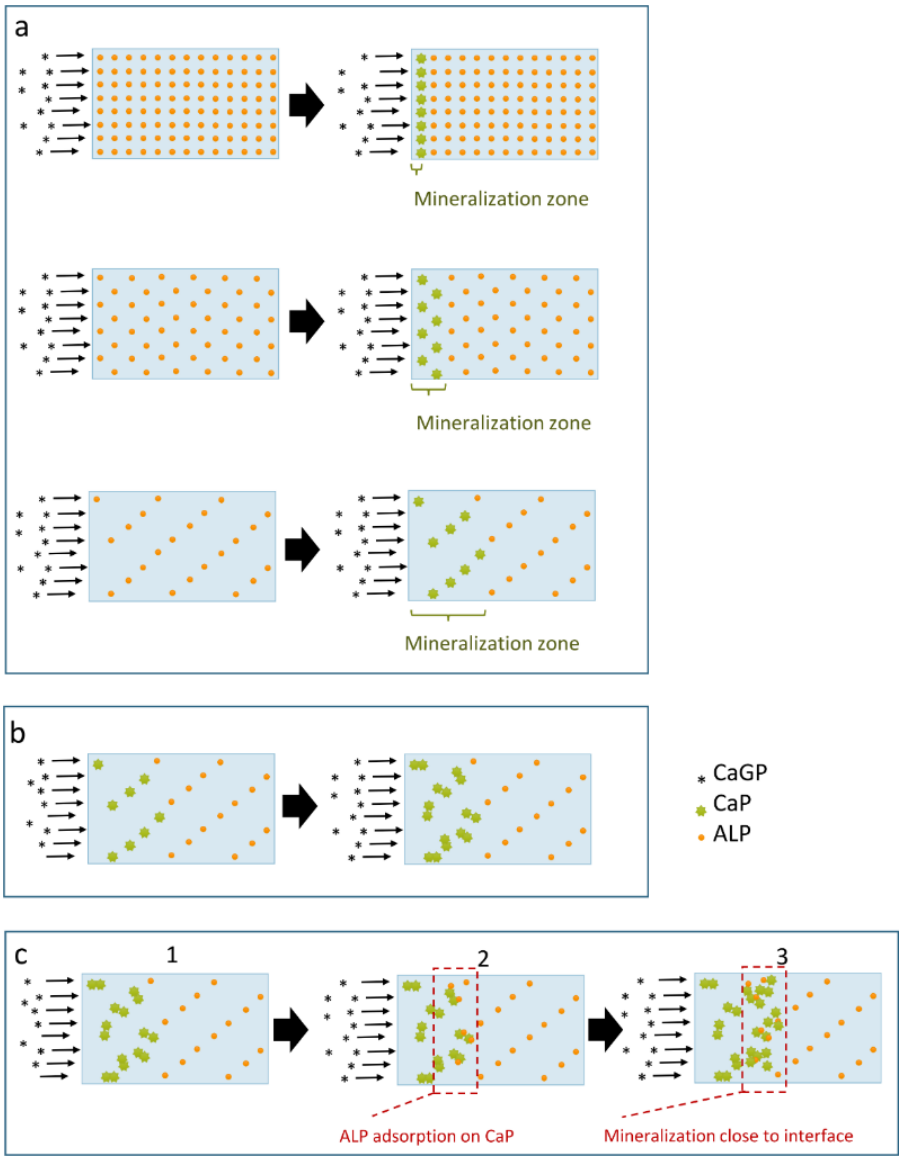

Fig. 8. Hypothetical formation of mineralization profiles in GG hydrogels. Depth of mineralization zone is strongly dependent on ALP concentration. Slower reaction due to lower ALP concentration allows for deeper CaGP diffusion (a). Mineral precipitates formed in mineralization zone act as further nucleation sites thus mineralization zone depth is not changing over time but CaP concentration increases (b). Adsorption of ALP on mineral deposits at the interface and acceleration of mineralization process on that region as a result CaP concentration increases (c).

A higher concentration of ALP, i.e., 5 mg/ml (see Fig. 2 (a-c)), resulted in an increased mineralization rate and produced a higher amount of CaP mineral, but the depth of mineralization was lower. In this case, CaGP diffusion was hindered, presumably because of a large amount of CaP precipitates. Furthermore, the CaGP substrate was consumed more rapidly by ALP present at high concentration before it could reach deeper parts of the hydrogel. The mineral formation for these types of samples is shown in Fig. 8 (a), line 1.

The blockage of diffusion might also be responsible for much deeper side surface mineralization of these samples (inorganic phosphate from CaGP was released close to the surface in this case). For lower concentrations of ALP, that is, 0.5 and 0.1 mg/ml (see Fig. 2 (d)-(i)), the enzymatic reaction was slower and the substrate was able to diffuse much deeper (Fig. 8 (a), lines 2 and 3). This effect of superficial mineralization, where the process is mostly limited to a few millimetres in depth and bulk of a material remains unchanged, was already presented in other studies where mineralization by urease was used [59] or where hydrogels were mineralized by alternate soaking [60]. The diffusion of molecules in hydrogels is related to the size of the mesh [61]. After CaP precipitation, the effective mesh size of the hydrogel might be lower and therefore the diffusion rate is decreasing. However, it is unclear if in this case the mineral part is closely connected to GG chains and makes it thicker, therefore decreasing the mesh size. The nanometer-sized particles located inside hydrogel pores are probably blocking diffusion and due to extensive surface area, may also be responsible for ALP adsorption. Douglas et al. showed that CaP particles inside the GG hydrogel can be as small as 15 nm [56].

An interesting fact is that the mineralization depth after one day was stable and was not progressing over time inside the hydrogel (except for 0.1 mg/ml of ALP). Only the level of mineralization was increasing. This was probably because the precipitates previously produced acted as nucleation sites for the new ones. The mineral formation for this type of sample is shown in Fig. 8 (b).

It is probable that other types of nucleation site were responsible for unusual precipitation on CaP inside the non-mineralized zone. In this case, the majority of CaP precipitated in the already mineralized part, but a small amount of ions at concentration below equilibrium solubility diffused deeper and presumably precipitated in small air bubbles or cracks inside the hydrogel (the solubility for dicalcium phosphate at pH = 7 is 4.8×10^{-2} g/dm^3 and for hydroxyapatite 3×10^{-4} g/dm^3) [62].

Additionally, the interface between the two phases also acted as a preferred site of nucleation for low-concentration ions in that region. ALP diffusing from deeper parts might be adsorbed on already precipitated CaP phases close to the interface, further accelerating its mineralization (Fig. 8 (c)). This is why the level of mineralization was much higher at the interface and also why this phenomenon was more prominent at later stages of the mineralization process. A similar phenomenon was observed when the thin layers of hydrogel were mineralized under a glass slide (Supplementary Figure 2).

Therefore, because of this unexpected phenomenon, not in every condition a gradient mineralization profile was possible. Blocking the diffusion caused the formation of an undesirable sharp transition, which is not preferable as the osteochondral junction. A sharp transition was also present in many cases inside the hydrogel close to the interface zone as this part was unexpectedly mineralized to a greater extent. Experimental data showed that the first effect can be reduced by lowering the concentration of ALP to 0.5 mg/ml. The second effect can be reduced by: (1) using a higher concentration of ALP , (2) increasing the concentration of GG, and (3) decreasing the process time. A sharp transition is also visible for samples prepared for SEM and Raman imaging (Fig. 3 and 4). In this case, the resulted transition was mostly related to the difference in water content between the mineralized and non-mineralized part. The shrinkage of the high amount of water containing nonmineralized part during sample preparation caused sample deformation, emphasizing the effect of a sharp transition. However, even on these images traces of mildly mineralized material close to the transition zone are visible.

Poor mineralization close to the top surface was observed for 0.1 mg/ml ALP samples and to a lesser extent for 0.5 mg/ml ALP samples. It was more likely related to rapid ALP diffusion from hydrogels. ALP can diffuse outside freely and was previously demonstrated that for 0.7% GG samples with 8 mm diameter and 4 mm thickness, 40% of the enzyme was released in 270 min [51]. A similar phenomenon has already been reported in our previous research [63]. For small cylindrical samples with low concentrations of ALP, mineralization mostly takes place inside the hydrogel as a result of the loss of ALP from the surface. Faster mineralization rates at the beginning for highly concentrated ALP samples must have prevented ALP depletion in further stages of mineralization.

0.7% GG samples with 0.5 mg/ml ALP mineralized for 3 days were further investigated as an example of intermediate mineralization level and relatively uniform mineralization profile. This sample composition was also investigated in our previous work [56,64]. For these samples, the mineralization level close to the surface was only slightly lower than in the rest of the volume, and there were also no CaP precipitates in the non-mineralized zone.

4.2. Modification of material properties and cell response

The goal of this study was to obtain distinctly chemically and mechanically different areas in one material: mineralized for bone and non-mineralized for cartilage. The non-mineralized part of the material remained unchanged. The mineralization of the bone-like part was achieved by diffusion-limited enzymatic mineralization. The formation of CaP inside the GG hydrogel was shown directly by EDX, FTIR, and Raman spectroscopy/imaging and indirectly by the increase in the dry mass percentage. The SEM and AFM images in dry state showed that the CaP crystals formed by this method were smaller than 1 µm. Evidence of the formation of apatite nanocrystals (15 nm in diameter) achieved by this method was demonstrated by Douglas et al. using XRD and TEM [56].

The AFM and SEM images of the mineralized hydrogel showed a rough surface with a globular structure and pores of less than 1 µm. This globular mineralization pattern was not the effect of freeze-drying because it was also visible for GG hydrogels in their native wet state (see Fig. 5 (c) (d)). Observed globules may arise from the inhomogeneity of the GG hydrogel at the nanoscale, which was also shown in this study. In our AFM measurement setup, resolution was too low to observe separated GG helices with thickness approximately 1 nm [65] and CaP crystals of 15 nm, therefore it is also not clear whether CaP particles are closely associated with GG or separated.

The stiffness distribution of the mineralized surface showed various values of Young's modulus, ranging from very low (< 1 kPa) to high (> 500 kPa). The E values for the mineralized hydrogel were characterized by an exponential distribution, while the non-mineralized material was characterized by a normal distribution. This would imply that non-mineralized material was homogenous at the micrometer scale range, while the mineralized exhibited a wide range of distinct E values depending on the level of mineralization in a particular place and also in the nearest surrounding. The median E value for the mineralized surface was more than 10 times higher than for the non-mineralized one. This increase was consistent with the bulk stiffness measurements of G' obtained by rheometry and E in the compression test. Two distinct zones of different stiffness obtained by the proposed method were expected to have a significant impact on cell differentiation into the bone or cartilage linage. As it was shown before, MSC differentiate into osteoblasts within the 62 to 68 kPa range [66] and chondrogenic differentiation of MSCs is promoted by soft substrates (0.5 kPa) [67].

Enzymatic mineralization of the GG hydrogel led to superior cell adhesion, as demonstrated by live/dead staining. In the first experiment (see Fig. 7 (a), (b), (c)) after day 4 almost the entire surface was covered by MG-63 cells; therefore, there was no further increase in viability after 8 days. Slight decrease in cell viability may be attributed to decreased metabolic activity after 8 days, which may be

characteristic for non-proliferating MG-63 cells, due to the lack of free surface for cells to adhere. For non-mineralized material, cells were growing mostly in clusters, which was caused by their poor adhesion to this substrate. Although chondrocytes were not tested, the morphology of MG-63 cells in this case was more similar to that characteristic of cartilage tissue [68]. In the second experiment (see Fig. 7 (d), (e)) cells seeded in the interface area were spreading and proliferating merely on the mineralized zone. It was presumably due to higher stiffness, higher roughness, and higher surface area as shown by others [54]. This was clearly demonstrated that by this kind of mineralization, material of two distinct zones can be obtained and that the chemical and mechanical properties at the interface act as strong signals for cells to attach, spread, and proliferate. This kind of sharp transition is considered beneficial characteristics in the case of osteochondral defect regeneration, where cell differentiation in two distinct lineages is desirable in a very close region (< 5 μm) [69].

Structural and mechanical differences alone are prerequisites to establish an effective transition between two different tissues, but the establishment of biochemical gradients, particularly in the interface region is also needed [70]. Therefore, further research is required. This biochemical gradient can be achieved by incorporating growth factors such as bone morphogenetic proteins (BMP) and nanoparticles loaded with transforming growth factor alpha (TGFα). Mineral nanocrystals can also act as a high surface absorber of growth factors [53].

4.3. Perspectives of enzymatic mineralization limited by diffusion

The monolithic hydrogel scaffold obtained by the limited substrate diffusion enzymatic mineralization method is a valuable alternative to achieve a mineral gradient inside the hydrogel material. It does not require the introduction of ceramic powder to the hydrogel prior to gelation, which may generate additional problems with agglomeration, sedimentation, inhomogeneous distribution, and the lowering of the mechanical strength of the scaffold. The method can potentially be adapted to other materials, as it is based on enzymatic mineralization that works in other biopolymers – fibrin, silk, whey protein isolate [55,71,72] to obtain material with better biological response and strength needed for osteochondral applications. The potential limiting factor of the presented method may be the depth of mineralized zone. However, in our experiments, depth of around 10 mm was achieved (however, only for low ALP concentration), therefore, in this case the obtained bone part is similar in size to existing commercial products [73].

Hydrogel osteochondral scaffolds produced by our method are intended to be used as a cell-free approach, which is increasingly popular as a more simple and reliable and low cost solution [6]. The presence of cells in the osteochondral scaffold is still debatable. The cell-free approach can

eliminate the need for cell source and legislative concerns [7]. Instead, cells may be recruited to scaffolds from surrounding tissues, as recently demonstrated with a hydrogel scaffold containing specific MSC recruiting aptamers [32] or affinity peptide sequences [35]. A similar acellular GG scaffold with mineralized alginate by the addition of HAP powder was successfully used to regenerate critical osteochondral defects in rabbits [34]. The large surface area of nanometric CaP particles inside the hydrogel can be potentially used to absorb bone specific molecules, thus creating not only CaP, but also other chemical gradients similarly to those present in osteochondral region [15].

In our method, the mineralization gradient profile and the stiffness of the material stiffness can be relatively easily by changing the ALP concentration and the time of the process. Therefore, the stiffness of the material can be adapted to chondrocyte and osteoblasts, or its adapted stiffness can induce differentiation of the MSC differentiation into chondritic or osteogenic linage [66,67]. The hydrogel scaffold should also provide the exchange of chemical signals between two layers necessary to facilitate a proper regeneration process [74]. From this perspective, a sharp transition on the interface obtained under many tested conditions is not preferable, as it indicates that diffusion of the low molecular substrate (CaGP) might have been blocked. The hydrogel structure after mineralization should still ensure diffusion of the necessary molecules. Therefore, a lower mineralization level and a more uniform gradient transition are preferable in this case.

Due to the simplicity of the proposed method, in the authors' opinion, it can be adapted to microfluidic devices to produce the organ-on-chip model of the osteochondral junction. First, the mineralization process can be conducted in a microfluidic cell in more controlled manner by providing the appropriate amount of CaGP substrate by microfluidics and due to the optical transparency of GG hydrogel. After the mineralization process, the gradient material can be seeded with cells and cultured owing to the architecture of the microfluidic chamber under two different conditions, i.e., dedicated to bone and cartilage parts. A similar idea of a dual-flow bioreactor that simulates the osteochondral junction has recently been explored [75].

This research presents a new approach to obtain a partially mineralized hydrogel with the use of enzymatic mineralization by limiting substrate diffusion. The scope of this research was to confirm the feasibility of mineral gradient formation and the positive relation between material stiffness and basic cell response. Therefore, the question of how the material obtained will act within the osteochondral defect is still open. More in-depth biological research that involves the differentiation of MSC and its characterisation by tissue-specific markers for bone and cartilage should provide a justification for our approach.

5. Conclusion

The substrate diffusion-limiting method for the enzymatic mineralization of GG proposed in this study allowed for the successful fabrication of biphasic monolithic GG hydrogels. Such hydrogels consist of the two phases: non-mineralized and mineralized. Parameters of the mineralization profile, such as depth and CaP content, were adjusted by ALP concentration, duration of the process, but less by GG concentration. The method was able to produce monolithic biphasic material with two zones with different chemical compositions, microstructures, and mechanical properties that were responsible for the specific biological response.

Acknowledgments

K.P. acknowledges European Society for Biomaterials for Racquel LeGeros Award, and FSS mobility program which supported his stay at ERRMECe Laboratory, University of Cergy-Pontoise, France and at Department of Biomaterials University of Oslo, Norway, respectively. This study was supported by the National Science Centre Poland (No 2018/29/N/ST8/01544) and by the program ”Excellence Initiative–Research University” for AGH University of Science and Technology, Kraków, Poland.

References

[1] Deng C, Chang J, Wu C. Bioactive scaffolds for osteochondral regeneration. J Orthop Transl 2019;17:15–25. https://doi.org/10.1016/j.jot.2018.11.006.
[2] Meng X, Ziadlou R, Grad S, Alini M, Wen C, Lai Y, et al. Animal Models of Osteochondral Defect for Testing Biomaterials. Biochem Res Int 2020;2020:1–12. https://doi.org/10.1155/2020/9659412.
[3] DeFroda SF, Bokshan SL, Yang DS, Daniels AH, Owens BD. Trends in the Surgical Treatment of Articular Cartilage Lesions in the United States from 2007 to 2016. J Knee Surg 2021;34:1609–16. https://doi.org/10.1055/s-0040-1712946.
[4] Frassica MT, Grunlan MA. Perspectives on Synthetic Materials to Guide Tissue Regeneration for Osteochondral Defect Repair. ACS Biomater Sci Eng 2020;6:4324–36. https://doi.org/10.1021/acsbiomaterials.0c00753.
[5] Panseri S, Russo A, Cunha C, Bondi A, Di Martino A, Patella S, et al. Osteochondral tissue engineering approaches for articular cartilage and subchondral bone regeneration. Knee Surg Sports Traumatol Arthrosc 2012;20:1182–91. https://doi.org/10.1007/s00167-011-1655-1.
[6] Boffa A, Solaro L, Poggi A, Andriolo L, Reale D, Di Martino A. Multi-layer cell-free scaffolds for osteochondral defects of the knee: a systematic review and meta-analysis of clinical evidence. J Exp Orthop 2021;8:56. https://doi.org/10.1186/s40634-021-00377-4.

[7] Ai C, Lee YHD, Tan XH, Tan SHS, Hui JHP, Goh JC-H. Osteochondral tissue engineering: Perspectives for clinical application and preclinical development. J Orthop Transl 2021;30:93–102. https://doi.org/10.1016/j.jot.2021.07.008.
[8] Zhang X, Liu Y, Zuo Q, Wang Q, Li Z, Yan K, et al. 3D Bioprinting of Biomimetic Bilayered Scaffold Consisting of Decellularized Extracellular Matrix and Silk Fibroin for Osteochondral Repair. Int J Bioprinting 2021;7:401. https://doi.org/10.18063/ijb.v7i4.401.
[9] Duan P, Pan Z, Cao L, Gao J, Yao H, Liu X, et al. Restoration of osteochondral defects by implanting bilayered poly(lactide-co-glycolide) porous scaffolds in rabbit joints for 12 and 24 weeks. J Orthop Transl 2019;19:68–80. https://doi.org/10.1016/j.jot.2019.04.006.
[10] Yang T, Tamaddon M, Jiang L, Wang J, Liu Z, Liu Z, et al. Bilayered scaffold with 3D printed stiff subchondral bony compartment to provide constant mechanical support for long-term cartilage regeneration. J Orthop Transl 2021;30:112–21. https://doi.org/10.1016/j.jot.2021.09.001.
[11] Peters AE, Akhtar R, Comerford EJ, Bates KT. The effect of ageing and osteoarthritis on the mechanical properties of cartilage and bone in the human knee joint. Sci Rep 2018;8:5931. https://doi.org/10.1038/s41598-018-24258-6.
[12] Trinity Centre for Bioengineering, Department of Mechanical Engineering, Parsons Building, Trinity College Dublin, Dublin 2, Ireland, Gannon A, Nagel T, Bell A, Avery N, Kelly D. Postnatal changes to the mechanical properties of articular cartilage are driven by the evolution of its collagen network. Eur Cell Mater 2015;29:105–23. https://doi.org/10.22203/eCM.v029a09.
[13] Antons J, Marascio MGM, Nohava J, Martin R, Applegate LA, Bourban PE, et al. Zone-dependent mechanical properties of human articular cartilage obtained by indentation measurements. J Mater Sci Mater Med 2018;29:57. https://doi.org/10.1007/s10856-018-6066-0.
[14] Nooeaid P, Salih V, Beier JP, Boccaccini AR. Osteochondral tissue engineering: scaffolds, stem cells and applications. J Cell Mol Med 2012;16:2247–70. https://doi.org/10.1111/j.1582-4934.2012.01571.x.
[15] Fu J-N, Wang X, Yang M, Chen Y-R, Zhang J-Y, Deng R-H, et al. Scaffold-Based Tissue Engineering Strategies for Osteochondral Repair. Front Bioeng Biotechnol 2022;9:812383. https://doi.org/10.3389/fbioe.2021.812383.
[16] Wei W, Dai H. Articular cartilage and osteochondral tissue engineering techniques: Recent advances and challenges. Bioact Mater 2021;6:4830–55. https://doi.org/10.1016/j.bioactmat.2021.05.011.
[17] Lin T-H, Wang H-C, Cheng W-H, Hsu H-C, Yeh M-L. Osteochondral Tissue Regeneration Using a Tyramine-Modified Bilayered PLGA Scaffold Combined with Articular Chondrocytes in a Porcine Model. Int J Mol Sci 2019;20:326. https://doi.org/10.3390/ijms20020326.
[18] Chicatun F, Rezabeigi E, Muja N, Kaartinen MT, McKee MD, Nazhat SN. A bilayered dense collagen/chitosan hydrogel to model the osteochondral interface. Emergent Mater 2019;2:245–62. https://doi.org/10.1007/s42247-019-00044-6.
[19] Liang X, Duan P, Gao J, Guo R, Qu Z, Li X, et al. Bilayered PLGA/PLGA-HAp Composite Scaffold for Osteochondral Tissue Engineering and Tissue Regeneration. ACS Biomater Sci Eng 2018;4:3506–21. https://doi.org/10.1021/acsbiomaterials.8b00552.
[20] Zhang W, Lian Q, Li D, Wang K, Hao D, Bian W, et al. The effect of interface microstructure on interfacial shear strength for osteochondral scaffolds based on biomimetic design and 3D printing. Mater Sci Eng C 2015;46:10–5. https://doi.org/10.1016/j.msec.2014.09.042.
[21] Asensio G, Benito-Garzón L, Ramírez-Jiménez RA, Guadilla Y, Gonzalez-Rubio J, Abradelo C, et al. Biomimetic Gradient Scaffolds Containing Hyaluronic Acid and Sr/Zn Folates for Osteochondral Tissue Engineering. Polymers 2021;14:12. https://doi.org/10.3390/polym14010012.
[22] Catoira MC, Fusaro L, Di Francesco D, Ramella M, Boccafoschi F. Overview of natural hydrogels for regenerative medicine applications. J Mater Sci Mater Med 2019;30:115. https://doi.org/10.1007/s10856-019-6318-7.
[23] Ng JY, Obuobi S, Chua ML, Zhang C, Hong S, Kumar Y, et al. Biomimicry of microbial polysaccharide hydrogels for tissue engineering and regenerative medicine – A review. Carbohydr Polym 2020;241:116345. https://doi.org/10.1016/j.carbpol.2020.116345.

[24] Hoffman AS. Hydrogels for biomedical applications. Adv Drug Deliv Rev 2012;64:18–23. https://doi.org/10.1016/j.addr.2012.09.010.
[25] Ullah F, Othman MBH, Javed F, Ahmad Z, Akil HMd. Classification, processing and application of hydrogels: A review. Mater Sci Eng C 2015;57:414–33. https://doi.org/10.1016/j.msec.2015.07.053.
[26] Chamkouri H. A Review of Hydrogels, Their Properties and Applications in Medicine. Am J Biomed Sci Res 2021;11:485–93. https://doi.org/10.34297/AJBSR.2021.11.001682.
[27] Correa S, Grosskopf AK, Lopez Hernandez H, Chan D, Yu AC, Stapleton LM, et al. Translational Applications of Hydrogels. Chem Rev 2021;121:11385–457. https://doi.org/10.1021/acs.chemrev.0c01177.
[28] Wei W, Ma Y, Yao X, Zhou W, Wang X, Li C, et al. Advanced hydrogels for the repair of cartilage defects and regeneration. Bioact Mater 2021;6:998–1011. https://doi.org/10.1016/j.bioactmat.2020.09.030.
[29] Lin H, Yin C, Mo A, Hong G. Applications of Hydrogel with Special Physical Properties in Bone and Cartilage Regeneration. Materials 2021;14:235. https://doi.org/10.3390/ma14010235.
[30] Xin W, Gao Y, Yue B. Recent Advances in Multifunctional Hydrogels for the Treatment of Osteomyelitis. Front Bioeng Biotechnol 2022;10:865250. https://doi.org/10.3389/fbioe.2022.865250.
[31] Chen Z, Xiao H, Zhang H, Xin Q, Zhang H, Liu H, et al. Heterogenous hydrogel mimicking the osteochondral ECM applied to tissue regeneration. J Mater Chem B 2021;9:8646–58. https://doi.org/10.1039/D1TB00518A.
[32] Yang Z, Zhao T, Gao C, Cao F, Li H, Liao Z, et al. 3D-Bioprinted Difunctional Scaffold for In Situ Cartilage Regeneration Based on Aptamer-Directed Cell Recruitment and Growth Factor-Enhanced Cell Chondrogenesis. ACS Appl Mater Interfaces 2021;13:23369–83. https://doi.org/10.1021/acsami.1c01844.
[33] Kilian D, Ahlfeld T, Akkineni AR, Bernhardt A, Gelinsky M, Lode A. 3D Bioprinting of osteochondral tissue substitutes – in vitro-chondrogenesis in multi-layered mineralized constructs. Sci Rep 2020;10:8277. https://doi.org/10.1038/s41598-020-65050-9.
[34] Xing J, Peng X, Li A, Chen M, Ding Y, Xu X, et al. Gellan gum/alginate-based Ca-enriched acellular bilayer hydrogel with robust interface bonding for effective osteochondral repair. Carbohydr Polym 2021;270:118382. https://doi.org/10.1016/j.carbpol.2021.118382.
[35] Huang B, Li P, Chen M, Peng L, Luo X, Tian G, et al. Hydrogel composite scaffolds achieve recruitment and chondrogenesis in cartilage tissue engineering applications. J Nanobiotechnology 2022;20:25. https://doi.org/10.1186/s12951-021-01230-7.
[36] Chen Y, Chen Y, Xiong X, Cui R, Zhang G, Wang C, et al. Hybridizing gellan/alginate and thixotropic magnesium phosphate-based hydrogel scaffolds for enhanced osteochondral repair. Mater Today Bio 2022;14:100261. https://doi.org/10.1016/j.mtbio.2022.100261.
[37] Lafuente-Merchan M, Ruiz-Alonso S, García-Villén F, Gallego I, Gálvez-Martín P, Saenz-del-Burgo L, et al. Progress in 3D Bioprinting Technology for Osteochondral Regeneration. Pharmaceutics 2022;14:1578. https://doi.org/10.3390/pharmaceutics14081578.
[38] Osmałek T, Froelich A, Tasarek S. Application of gellan gum in pharmacy and medicine. Int J Pharm 2014;466:328–40. https://doi.org/10.1016/j.ijpharm.2014.03.038.
[39] Costa L, Silva-Correia J, Oliveira JM, Reis RL. Gellan Gum-Based Hydrogels for Osteochondral Repair. In: Oliveira JM, Pina S, Reis RL, San Roman J, editors. Osteochondral Tissue Eng., vol. 1058, Cham: Springer International Publishing; 2018, p. 281–304. https://doi.org/10.1007/978-3-319-76711-6_13.
[40] Chen M, Yu P, Xing J, Wang Y, Ren K, Zhou G, et al. Gellan gum modified hyaluronic acid hydrogels as viscosupplements with lubrication maintenance and enzymatic resistance. J Mater Chem B 2022;10:4479–90. https://doi.org/10.1039/D2TB00421F.
[41] Leone G, Consumi M, Pepi S, Pardini A, Bonechi C, Tamasi G, et al. Enriched Gellan Gum hydrogel as visco-supplement. Carbohydr Polym 2020;227:115347. https://doi.org/10.1016/j.carbpol.2019.115347.

[42] Akkineni AR, Elci BS, Lode A, Gelinsky M. Addition of High Acyl Gellan Gum to Low Acyl Gellan Gum Enables the Blends 3D Bioprintable. Gels 2022;8:199. https://doi.org/10.3390/gels8040199.
[43] Mouser VHM, Melchels FPW, Visser J, Dhert WJA, Gawlitta D, Malda J. Yield stress determines bioprintability of hydrogels based on gelatin-methacryloyl and gellan gum for cartilage bioprinting Biofabrication 2016, 19;8(3):035003. doi: 10.1088/1758-5090/8/3/035003
[44] Douglas TEL, Messersmith PB, Chasan S, Mikos AG, de Mulder ELW, Dickson G, et al. Enzymatic Mineralization of Hydrogels for Bone Tissue Engineering by Incorporation of Alkaline Phosphatase: Enzymatic Mineralization of Hydrogels for Bone Tissue Engineering by …. Macromol Biosci 2012;12:1077–89. https://doi.org/10.1002/mabi.201100501.
[45] Douglas TEL, Łapa A, Samal SK, Declercq HA, Schaubroeck D, Mendes AC, et al. Enzymatic, urease-mediated mineralization of gellan gum hydrogel with calcium carbonate, magnesium-enriched calcium carbonate and magnesium carbonate for bone regeneration applications: Hydrogels enzymatically mineralized with Ca/Mg-carbonate. J Tissue Eng Regen Med 2017;11:3556–66. https://doi.org/10.1002/term.2273.
[46] Zhang Y, Shu T, Wang S, Liu Z, Cheng Y, Li A, et al. The Osteoinductivity of Calcium Phosphate-Based Biomaterials: A Tight Interaction With Bone Healing. Front Bioeng Biotechnol 2022;10:911180. https://doi.org/10.3389/fbioe.2022.911180.
[47] Wang L, Huang Y, Ding K, Lai Y, Mao R, Luo F, et al. Polyphosphate enhanced biomimetic mineralization of 3D printing scaffolds for bone regeneration. Compos Part B Eng 2022;239:109989. https://doi.org/10.1016/j.compositesb.2022.109989.
[48] Lopez-Heredia MA, Łapa A, Reczyńska K, Pietryga K, Balcaen L, Mendes AC, et al. Mineralization of gellan gum hydrogels with calcium and magnesium carbonates by alternate soaking in solutions of calcium/magnesium and carbonate ion solutions. J Tissue Eng Regen Med 2018;12:1825–34. https://doi.org/10.1002/term.2675.
[49] Gkioni K, Leeuwenburgh SCG, Douglas TEL, Mikos AG, Jansen JA. Mineralization of Hydrogels for Bone Regeneration. Tissue Eng Part B Rev 2010;16:577–85. https://doi.org/10.1089/ten.teb.2010.0462.
[50] Yao J, Fang W, Guo J, Jiao D, Chen S, Ifuku S, et al. Highly Mineralized Biomimetic Polysaccharide Nanofiber Materials Using Enzymatic Mineralization. Biomacromolecules 2020;21:2176–86. https://doi.org/10.1021/acs.biomac.0c00160.
[51] Douglas T, Wlodarczyk M, Pamula E, Declercq H, de Mulder E, Bucko M, et al. Enzymatic mineralization of gellan gum hydrogel for bone tissue-engineering applications and its enhancement by polydopamine: Enzymatic mineralization of gellan gum enhanced by polydopamine functionalization. J Tissue Eng Regen Med 2014;8:906–18. https://doi.org/10.1002/term.1616.
[52] Guo Y, Du S, Quan S, Jiang F, Yang C, Li J. Effects of biophysical cues of 3D hydrogels on mesenchymal stem cells differentiation. J Cell Physiol 2021;236:2268–75. https://doi.org/10.1002/jcp.30042.
[53] Qiu Y, Xu X, Guo W, Zhao Y, Su J, Chen J. Mesoporous Hydroxyapatite Nanoparticles Mediate the Release and Bioactivity of BMP-2 for Enhanced Bone Regeneration. ACS Biomater Sci Eng 2020;6:2323–35. https://doi.org/10.1021/acsbiomaterials.9b01954.
[54] Wei S, Deng Y, Liu X, Xu A, Wang L, Luo Z, et al. Effect of surface roughness on osteogenesis in vitro and osseointegration in vivo of carbon fiber-reinforced polyetheretherketone–nanohydroxyapatite composite. Int J Nanomedicine 2015:1425. https://doi.org/10.2147/IJN.S75557.
[55] Douglas TEL, Gassling V, Declercq HA, Purcz N, Pamula E, Haugen HJ, et al. Enzymatically induced mineralization of platelet-rich fibrin. J Biomed Mater Res A 2012;100A:1335–46. https://doi.org/10.1002/jbm.a.34073.
[56] Douglas TEL, Krawczyk G, Pamula E, Declercq HA, Schaubroeck D, Bucko MM, et al. Generation of composites for bone tissue-engineering applications consisting of gellan gum hydrogels mineralized with calcium and magnesium phosphate phases by enzymatic means: Gellan gum

and calcium and magnesium phosphate composites. J Tissue Eng Regen Med 2016;10:938–54. https://doi.org/10.1002/term.1875.
[57] Flores-Merino MV, Chirasatitsin S, LoPresti C, Reilly GC, Battaglia G, Engler AJ. Nanoscopic mechanical anisotropy in hydrogel surfaces. Soft Matter 2010;6:4466. https://doi.org/10.1039/c0sm00339e.
[58] Silva-Correia J, Oliveira JM, Caridade SG, Oliveira JT, Sousa RA, Mano JF, et al. Gellan gum-based hydrogels for intervertebral disc tissue-engineering applications. J Tissue Eng Regen Med 2011;5:e97–107. https://doi.org/10.1002/term.363.
[59] Milovanovic M, Mihailowitsch L, Santhirasegaran M, Brandt V, Tiller JC. Enzyme-induced mineralization of hydrogels with amorphous calcium carbonate for fast synthesis of ultrastiff, strong and tough organic–inorganic double networks. J Mater Sci 2021;56:15299–312. https://doi.org/10.1007/s10853-021-06204-6.
[60] Nonoyama T. Robust hydrogel–bioceramics composite and its osteoconductive properties. Polym J 2020;52:709–16. https://doi.org/10.1038/s41428-020-0332-y.
[61] Axpe E, Chan D, Offeddu GS, Chang Y, Merida D, Hernandez HL, et al. A Multiscale Model for Solute Diffusion in Hydrogels. Macromolecules 2019;52:6889–97. https://doi.org/10.1021/acs.macromol.9b00753.
[62] Wu VM, Uskoković V. Is there a relationship between solubility and resorbability of different calcium phosphate phases in vitro ? Biochim Biophys Acta BBA - Gen Subj 2016;1860:2157–68. https://doi.org/10.1016/j.bbagen.2016.05.022.
[63] Pietryga K, Costa J, Pereira P, Douglas TEL, Pamula E. Promotion of bone cel growth on gellan gum hydrogels by enzymatic mineralization, Eng Biomat 2014;125:6–12.
[64] Douglas TEL, Dokupil A, Reczyńska K, Brackman G, Krok-Borkowicz M, Keppler JK, et al. Enrichment of enzymatically mineralized gellan gum hydrogels with phlorotannin-rich *Ecklonia cava* extract Seanol ® to endow antibacterial properties and promote mineralization. Biomed Mater 2016;11:045015. https://doi.org/10.1088/1748-6041/11/4/045015.
[65] Morris ER, Nishinari K, Rinaudo M. Gelation of gellan – A review. Food Hydrocoll 2012;28:373–411. https://doi.org/10.1016/j.foodhyd.2012.01.004.
[66] Sun M, Chi G, Li P, Lv S, Xu J, Xu Z, et al. Effects of Matrix Stiffness on the Morphology, Adhesion, Proliferation and Osteogenic Differentiation of Mesenchymal Stem Cells. Int J Med Sci 2018;15:257–68. https://doi.org/10.7150/ijms.21620.
[67] Zhou Y, Qiu J, Wan L, Li J. The effect of matrix stiffness on the chondrogenic differentiation of mesenchymal stem cells. J Mol Histol 2022;53:805–16. https://doi.org/10.1007/s10735-022-10094-6.
[68] Karim A, Amin AK, Hall AC. The clustering and morphology of chondrocytes in normal and mildly degenerate human femoral head cartilage studied by confocal laser scanning microscopy. J Anat 2018;232:686–98. https://doi.org/10.1111/joa.12768.
[69] Campbell SE, Ferguson VL, Hurley DC. Nanomechanical mapping of the osteochondral interface with contact resonance force microscopy and nanoindentation. Acta Biomater 2012;8:4389–96. https://doi.org/10.1016/j.actbio.2012.07.042.
[70] Di Luca A, Van Blitterswijk C, Moroni L. The osteochondral interface as a gradient tissue: From development to the fabrication of gradient scaffolds for regenerative medicine: The Osteochondral Interface as a Gradient Tissue. Birth Defects Res Part C Embryo Today Rev 2015;105:34–52. https://doi.org/10.1002/bdrc.21092.
[71] Samal SK, Dash M, Declercq HA, Gheysens T, Dendooven J, Voort PVD, et al. Enzymatic Mineralization of Silk Scaffolds: Enzymatic Mineralization of Silk Scaffolds. Macromol Biosci 2014;14:991–1003. https://doi.org/10.1002/mabi.201300513.
[72] Norris K, Kocot M, Tryba AM, Chai F, Talari A, Ashton L, et al. Marine-Inspired Enzymatic Mineralization of Dairy-Derived Whey Protein Isolate (WPI) Hydrogels for Bone Tissue Regeneration. Mar Drugs 2020;18:294. https://doi.org/10.3390/md18060294.

[73] Drobnič M, Kolar M, Verdonk P, Vannini F, Robinson D, Altschuler N, et al. Complex Osteochondral Lesions of the Talus Treated With a Novel Bi-Phasic Aragonite-based Implant. J Foot Ankle Surg 2021;60:391–5. https://doi.org/10.1053/j.jfas.2020.06.028.
[74] Goldring SR, Goldring MB. Changes in the osteochondral unit during osteoarthritis: structure, function and cartilage–bone crosstalk. Nat Rev Rheumatol 2016;12:632–44. https://doi.org/10.1038/nrrheum.2016.148.
[75] Banh L, Cheung KK, Chan MWY, Young EWK, Viswanathan S. Advances in organ-on-a-chip systems for modelling joint tissue and osteoarthritic diseases. Osteoarthritis Cartilage 2022;30:1050–61. https://doi.org/10.1016/j.joca.2022.03.012.

Appendix

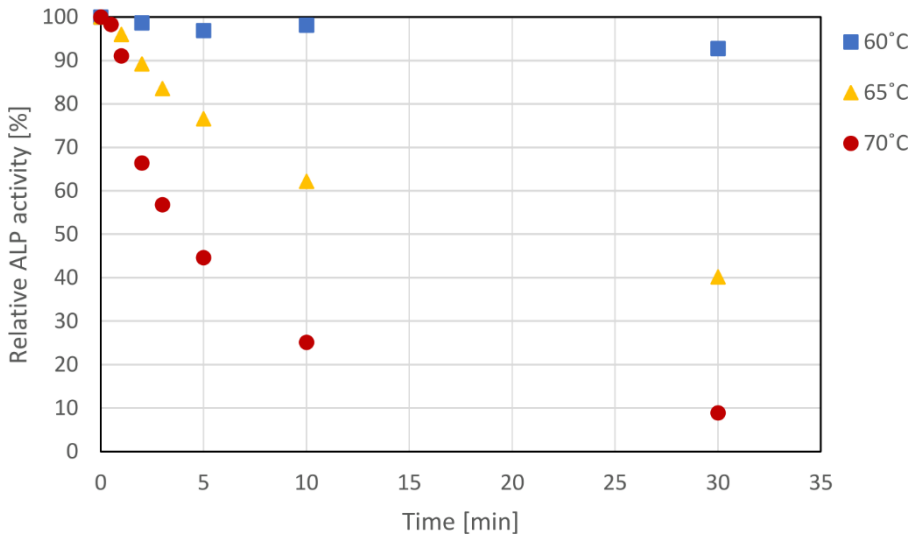

Supplementary Figure 1. ALP activity loss after incubation in high temperature conditions over time (relative to freshly made ALP solution.

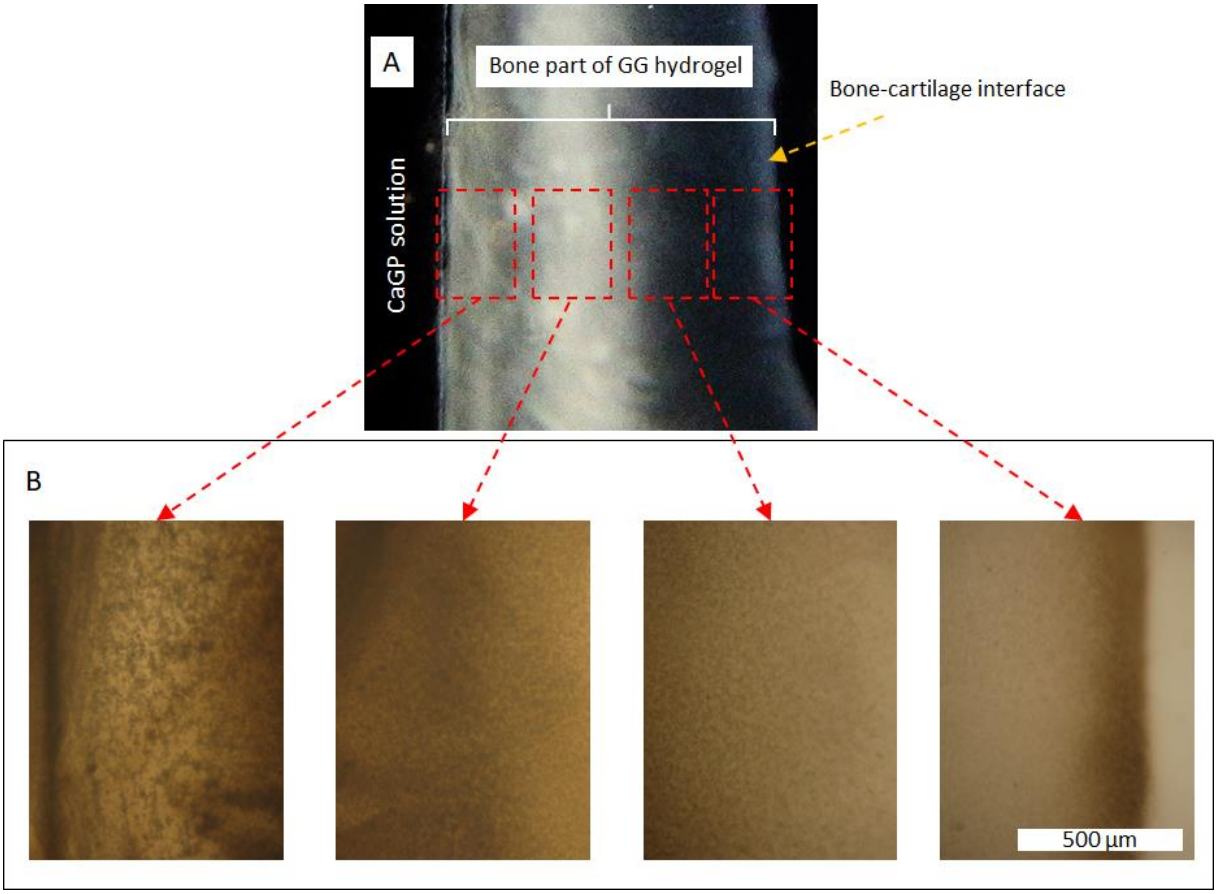

Supplementary Figure 2. Mineralization process in thin layer of hydrogel under glass slide after 3 days. Microphotography in reflected light (low magnification) and transmitted light (higher magnification) (B). Densification of mineralization process on interface is in this case also visible.

Biphasic monolithic osteochondral scaffolds obtained by diffusion-limited enzymatic mineralization of gellan gum hydrogel

Krzysztof Pietryga[1,], Katarzyna Reczyńska-Kolman[1], Janne E. Reseland[2], Håvard Haugen[2], Véronique Larreta-Garde[3], Elżbieta Pamuła[1*]

[1] AGH University of Science and Technology, Faculty of Materials Science and Ceramics, Department of Biomaterials and Composites, Al. Mickiewicza 30, 30-059 Kraków, Poland
[2] University of Oslo, Institute for Clinical Dentistry, Department of Biomaterials, PO Box 1109 Blindern, NO-0317 Oslo, Norway
[3] University of Cergy Pontoise, Biology Department, ERRMECe Laboratory, Cergy-Pontoise, 1 rue Descartes, 95000 Neuville-sur-Oise, France

*Corresponding author: epamula@agh.edu.pl

Biphasic monolithic osteochondral scaffolds obtained by diffusion-limited enzymatic mineralization of gellan gum hydrogel

Abstract

Biphasic monolithic materials for the treatment of osteochondral defects were produced from polysaccharide hydrogel, gellan gum (GG). GG was enzymatically mineralized by alkaline phosphatase (ALP) in the presence of calcium glycerophosphate (CaGP). The desired distribution of the calcium phosphate (CaP) mineral phase was achieved by limiting the availability of CaGP to specific parts of the GG sample. Therefore, mineralization of GG was facilitated by the diffusion of CaGP, causing the formation of the CaP gradient. The distribution of CaP was analyzed along the cross section of the GG. The formation of a CaP gradient was mainly affected by the mineralization time and the ALP concentration. The formation of CaP was confirmed by Fourier transform infrared spectroscopy (FTIR), Raman spectroscopy and mapping, as well as energy-dispersive X-ray spectroscopy (EDX) mapping of the interphase. The microstructure of mineralized and non-mineralized parts of the material was characterized by scanning electron microscopy (SEM) and atomic force microscopy (AFM) showing sub-micrometer CaP crystal formation, resulting in increased surface roughness. Compression tests and rheometric analyzes showed a 10-fold increase in stiffness of the GG mineralized part. Concomitantly, micromechanical tests performed by AFM showed an increase of Young's modulus from 17.8 to more than 200 kPa. *In vitro* evaluation of biphasic scaffolds was performed in contact with osteoblast-like MG-63 cells. The mineralized parts of GG were preferentially colonized by the cells over the non-mineralized parts. The results showed that osteochondral scaffolds of the desired structure and properties can be made from GG using a diffusion-limited enzymatic mineralization method.

Keywords: biomaterials; tissue engineering; osteochondral; hydrogel; mineralization;

1. Introduction

Osteochondral defects involving structural damage to the articular cartilage and the underlying subchondral bone result in serious disability for millions of people worldwide [1,2]. For example, knee cartilage surgical techniques were performed in almost 36 thousand patients in the United States between 2007 and 2016 [3]. To date, all clinically accepted methods have been shown to have limited capacity to treat severe osteochondral lesions. Currently available techniques, such as debridement, mosaicplasty, microfracture, and implantation of autologous chondrocytes are considered short-term clinical solutions; therefore, the development of regenerative medicine and tissue engineering (TE) approaches is needed for both articular cartilage and subchondral bone [4,5].

Scaffolds for osteochondral regeneration are categorized into three types: monophasic, biphasic, and multiphasic. In monophasic scaffolds, the material is homogenous throughout the whole construct. Biphasic and multiphasic scaffolds are currently more popular approaches for providing the specific microenvironment for cartilage and bone regeneration. Commercially available scaffolds for osteochondral regenerations are: multiphasic MaioRegen® (Finceramica, Italy), biphasic TruFit® (Smith & Nephew, USA), biphasic Biomatrix™ CRD (Arthrex, USA), biphasic Agili-C™ (CartiHeal, Israel) [6]. There is still no clear consensus on the optimal scaffold design for osteochondral repair. The advantage of monophasic scaffolds is a relatively easy fabrication process. Experimental evidence indicates the superiority of biphasic and multiphasic designs over monophasic scaffolds, as they can mimic hierarchical structure of osteochondral tissue [7]. The most popular approach in research currently is the combination of two parts that mimic cartilage and bone regions [8–10].

The difference in composition and mechanical properties between bone and cartilage makes scaffold design and fabrication challenging. The compressive modulus of the subchondral bone ranges from 11 to 15 GPa [11]. The compressive modulus of the hyaline cartilage and the deep zones of the cartilage is 0.2-2 and 10 MPa, respectively [12,13]. The preparation of TE scaffolds should take into account different mechanical, physicochemical, and biological requirements for the material to regenerate cartilage and bone parts and preserve their integrity at the same time. The scaffold should act as an extracellular matrix (ECM) that provides spatial and temporal clues that promote individual growth of cartilage and bone tissues [14,15].

Over the years, many strategies have been investigated to create bilayer scaffolds for osteochondral application, but generally a mixture of several kinds of biomaterials with different additives is common in designing both layers. The cartilaginous layer is made of hydrogels based on natural or synthetic origin due to viscoelastic similarity to the native extracellular matrix (ECM), while

the lower subchondral layer is made of stronger materials such as bioceramics, metals, and harder polymers [16]. Many types of bilayer scaffolds have been investigated for osteochondral applications, containing different materials: natural polymers (collagen, glycosaminoglycans, chitosan, starch, hyaluronic acid, alginate, gellan gum), synthetic polymers (polylactide, polyglicolide, poly(lactide-co-glycolide), poly-ε-caprolactone), ceramics (hydroxyapatite, tricalcium phosphate, Bioglass®) and metals [5,17–19].

Integration between the chondral and bone layers in the osteochondral scaffold is of key importance. Poor integration may lead to delamination and final failure during tissue regeneration[20]. From this point of view, the best strategy is to produce a monolithic scaffold with tightly integrated parts made of the same or similar base material (only with different additives) or gradient material with gradually changing mechanical, chemical, and biological parameters [21].

Materials of recently increasing interest in biomedical applications are hydrogels [22–24]. Hydrogels are formed from three-dimensional physically or chemically cross-linked water binding networks [25]. The advantages of hydrogels include high similarity to natural ECM, good injectability, precise fitting to the defect site, and the feasibility of incorporation of bioactive molecules (e.g., growth factors) and cells, and finally good diffusion of nutrients and waste products [26,27]. Hydrogels have been considered mainly in soft tissue engineering, although their versatility has resulted in TE of their application in bone, cartilage [28–30] and for osteochondral applications [31–37].

Gellan gum (GG) is a calcium-cross-linkable polysaccharide hydrogel produced by bacteria (*Sphingomonas elodea*). GG has been applied in the food and pharmaceutical industries, as well as in controlled drug delivery. The advantages of GG are its low cost, high biocompatibility, biodegradability, and low toxicity of by-products and also the fact that it is not animal-derived, avoiding regulatory concerns [38]. More recently, GG has been considered a promising biomaterial for cartilage regeneration and treatment as injectable viscosupplement substituting hyaluronic acid [39–41]. The advantage of GG for cartilage tissue application is the structural similarity to the natural glycosaminoglycans (GAG) that make up cartilage. Regarding bone application, GG has recently gained interest due to its high affinity for calcium ions and its ability to be mineralized [39]. Mesenchymal stem cells inside the GG blends were recently printed using the extrusion method showing viability above 80% [42]. The osteochondral scaffold produced from GG and sodium alginate (for the chondral part) and GG with hydroxyapatite or magnesium phosphate (for the bone part) were used to regenerate rabbit osteochondral defects [34,36]. Printable bioink from GelMA-GG blends laden with primary chondrocytes supported chondrogenesis and deposition of cartilaginous matrix [43].

Mineralization with calcium phosphate (CaP) can be used to adapt hydrogels such as GG for bone regeneration purposes [44,45]. The osteoinductivity of different CaP biomaterials for bone regeneration was discussed in a review [46]. The most common way to obtain hydrogel with a mineral component is by adding ceramic powder to the hydrogel solution prior to gelation. The mineralization of the hydrogel can also be obtained by physical precipitation of insoluble phosphate within the hydrogel matrix – SBF [47] soaking or alternate soaking [48]. Another way to achieve mineralization of hydrogels is through enzymatic means [49,50].

GG was mineralized by incorporation of an enzyme, alkaline phosphatase (ALP) and incubation in solutions containing calcium ions and organic phosphate groups, e.g., calcium glycerophosphate (CaGP). ALP uses CaGP as a substrate, cleaving phosphate and thus increasing its local concentration, allowing precipitation of insoluble CaP [51]. The presence of mineral phase in a hydrogel matrix was found to improve bioactivity and biocompatibility with bone tissue, increased affinity for biologically active molecules (growth factors, interleukins), and modified mechanical properties [44,52,53]. Furthermore, the increase in roughness and stiffness caused by mineralization promoted cell differentiation toward the osteoblastic phenotype, providing a more appropriate environment for the formation of subchondral bone [54]. The physical and biological properties of enzymatically mineralized GG and other hydrogels for bone regeneration purposes studied by Douglas *et al*. resulted in a more than five-time increase in the storage modulus and a three-time increase in Young's modulus. The presence of CaP in mineralized samples promoted the attachment and vitality of osteoblastic MC3T3-E1 cells [44,51,55,56].

The purpose of this study was to produce a monolithic gradient or a bilayer scaffold for osteochondral applications using selective enzymatic mineralization of the GG hydrogel. We hypothesize that to develop a mineral gradient, the availability of a mineralizing substrate (i.e., CaGP) can be spatially limited to the specific sample surface. Therefore, by relaying on CaGP diffusion into the hydrogel, one part of the material supplied by CaGP should undergo mineralization, while the other part should remain unaltered. By this original approach, monolithic materials with gradually changing chemical composition, microstructure, and biological properties can be produced. The proposed method eliminates the need to combine two different materials and reduces the risk of delamination. The proposed method is also simple and low cost. We hypothesize that the biomimetic mineralization utilized in the process will lead to a more homogeneous distribution of the mineral phase and polymer-ceramic integration similar to that that naturally occurred in bone.

In particular, in this study, our objective is to: 1) investigate the usefulness of this innovative method to fabricate biphasic osteochondral scaffold, 2) find a correlation between the mineralization

parameters and the gradient profile of the mineral phase, 3) evaluate how the mineralization level affects the microstructure and mechanical properties of the resulting material, and 4) assess the biological response of model osteoblast-like cells cultured on biphasic materials.

2. Materials and methods

2.1. Materials

All materials, including 'low-acyl' GG (Gelzan™CM, G1910), ALP (P7640) and CaGP (50043) were obtained from Sigma-Aldrich, unless otherwise noted.

2.2. Hydrogel preparation

Hydrogels were prepared by heating GG solution to 90 °C and addition of $CaCl_2$ as a cross-linker. The final $CaCl_2$ concentration in the samples was 0.03% w/v. After cooling to 60 °C, an aqueous solution of ALP was added to the final concentration of 2.5 mg/ml. Gel casting was performed immediately after ALP addition to minimize loss of ALP activity. It was also demonstrated (Appendix: Supplementary Figure) that ALP retains more than 90% activity at 60 °C for 30 min, but quickly loses its activity at temperatures higher than 65 °C. The gel preparation at a temperature higher than 50 °C (proposed by Douglas [55]) allowed more concentrated GG hydrogels to be produced.

The biphasic hydrogel samples were prepared as described above; however, the hydrogel was casted into the wells of a 24-well plate and covered with glass slides providing a flat surface without meniscus. After gelation, glass slides were removed. For AFM experiments, gel solution was casted into polyethylene (PE) ring (f = 10 mm, h = 1 mm) glued to glass slide (bottom part of the liquid cell of the AFM apparatus) and then covered with glass cover-slip providing flat top surface. The samples were then left for 30 min at 4 °C for gelation. Subsequently, the glass coverslip was gently removed. For FTIR, SEM, mechanical and rheology tests the samples were casted into Petri dish and after gelation cylinders of 12 or 25 mm in diameter and 4 and 2 mm in height, respectively, were cut.

2.3. Mineralization

GG samples were enzymatically mineralized using ALP and CaGP as a substrate. ALP increases mineral deposition by cleavage of the phosphate group from organic phosphate, thereby increasing the local phosphate concentration and enabling precipitation of the CaP phase inside the material. Calcium and glycerophosphate ions diffuse into the hydrogel matrix containing ALP. Cleaved

phosphate ions react with calcium ions to form insoluble CaP, which remains trapped within the gel. The by-product glycerol is released into the surrounding environment (Fig. 1(a)).

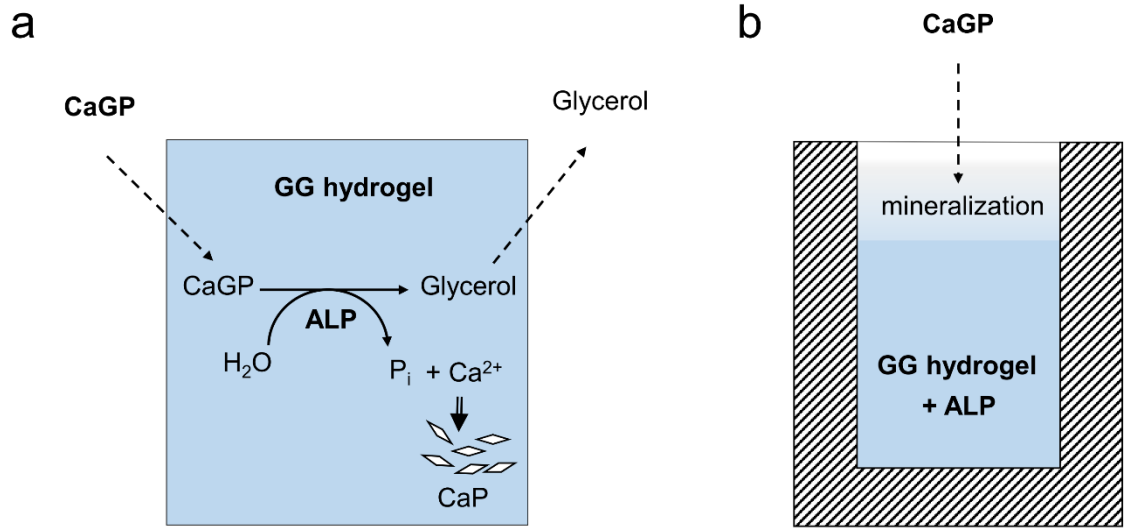

Fig. 1 Bulk enzymatic mineralization of GG hydrogel by ALP and CaGP (a) and diffusion-limited enzymatic mineralization used to obtain biphasic osteochondral scaffolds (b).

The samples were incubated in 0.1 M CaGP (prepared by dissolving CaGP powder in ddH_2O followed by 30 min of ultrasonication) at room temperature for 1 and 72 h. For micromechanical tests and surface topography by AFM, the mineralization was carried out by submerging the glass slides with PE rings containing a hydrogel in 0.1 M CaGP. The CaGP solution was changed every day. After mineralization, the samples were rinsed and subsequently incubated in ddH_2O for 1 day to remove residual CaGP. Nonmineralized hydrogels were used as controls.

Biphasic monolithic scaffold were obtained by exposing only the top part of cylindrical samples casted into a 24-well cell culture plate to CaGP mineralizing solution (Fig. 1(b)). The samples were partially mineralized because of the limitation of CaGP diffusion to deeper parts of the material caused by mineral formation. A GG hydrogel of different concentrations (0.7, 1.0 and 1.3%) and ALP content (0.1 – 5.0 mg/ml) were prepared. The samples were mineralized for 24, 72 and 168 h.

2.4. Determination of CaP content

To determine dry mass, which is a parameter that describes CaP content within hydrogels, the samples were weighted, dried for 48 h, and again weighted. The dry mass percentage was calculated as follows:

$$\text{Dry mass } (\%) = \frac{\text{weight after incubation and drying}}{\text{weight after incubation before drying}} * 100\%$$

The content of CaP was calculated by subtracting the theoretical dry mass % of GG (that is, 0.7%, 1%, 1.3%) from the dry mass (%) for each sample. For each type of material, 4 samples were tested. To determine the CaP profile along the direction of mineralization gradient, series of round slices (0.8 mm thick) were cut from cylindrical samples. The CaP content for each slice was determined as described before.

2.5. Scanning electron microscopy (SEM) and energy dispersive X-ray (EDX) spectroscopy

SEM analysis was performed on a TM3030 tabletop microscope (Hitachi, Tokyo, Japan) with EDX analyzer (Bruker Quantax 70, Billerica, Massachusetts, United States). Before SEM analysis, the samples were freeze dried for 24 h, attached to the holder by carbon sticky tape, and coated with a thin gold layer (Cressington 108 Sputter Coater, Watford, UK). In the case of EDX analysis, samples were studied without coating. Images were collected at a 15 kV acceleration voltage. To obtain high-resolution SEM images backscatter electron detector (BSD) mode in Gemini SEM 500 (Zeiss, Jena, Germany) was used.

2.6. Fourier transform infrared (FTIR) spectroscopy and Raman spectroscopy

After mineralization and drying (37 °C, 48 h), the molecular structure of the samples was examined by ATR-FTIR attenuated total reflectance. FTIR transmittance spectra were acquired using a Tensor 27 spectrometer (Bruker) equipped with standard Pike ATR cell and diamond ATR crystal. Spectra were recorded over the range 4000–525 cm^{-1} at a resolution of 4 cm^{-1} for 64 accumulations.

For Raman spectroscopy and mapping the samples were prepared as a thin (< 1 mm) slice, dried (37 °C, 48 h) and attached to the glass slide with two-sided sticky tape (carbon tape). Raman spectra for mineralized and non-mineralized parts of the sample were recorded using RISE Raman microscopy (WITec, Ulm, Germany). Raman maps were obtained by collecting spectra from 500 µm x 200 µm fragment and 20 μm^2 resolution. Data were processed using Project FOUR 4.1 software to obtain a distribution map for phosphate corresponding to the band at 963 cm^{-1}.

2.7. Mechanical properties

Mineralized hydrogels (samples 12 mm in diameter and 4 mm in height) were subjected to compression testing using ZWICK 1435 (Zwick Roell, Ulm, Germany). Hydrogels were placed between

piston heads and displacement was applied at a rate of 1 mm/min until the samples were compressed to 10% of their original height. Young's modulus (E) was determined on the stress-strain curve. For each sample group, 4 samples were tested.

Rheological measurements were made on an MCR 301 rheometer (Anton Paar, Graz, Austria) in parallel plate geometry equipped with a PP25 rotating head of diameter 25 mm. Samples 25 mm in diameter and 1 mm in height were tested in triplicate. Storage modulus (G') and loss modulus (G'') values were recorded at a frequency of 1.0 Hz and 0.1% strain.

2.8. Atomic force microscopy (AFM) imaging

Experiments were performed on dried hydrogels as well as hydrated hydrogels surrounded by deionized water (Millipore) on an MFP-3D atomic force microscope (Asylum Research, Oxford Instruments Company, Santa Barbara, CA) in liquid cell (Portless Fluid Dish Accessory for the MFP-3D™ AFM) with the use of an AC240TS cantilever at 21^{o}C.

Dry samples were imaged in dynamic force mode (AC mode) and contact mode. Three sample types were studied: unmodified 0.7% GG gel, 0.7% GG gel containing 2.5 mg/ml ALP mineralized for 1 h and 0.7% GG gel containing 2.5 mg/ml ALP mineralized for 72 h. Flat films of dried gels were attached to glass slide by sticky tape. Each cantilever was calibrated in air with Get REAL in Igor 15.0 software. The calibration protocol measured the thermal noise spectrum and on the basis of the Sader method, the spring constant and invOLS were acquired. The images were collected with low scanning rate (0.2 Hz) and low setpoint (20-70 mV).

Hydratated hydrogel was imaged in AC mode, covered by deionized water in the liquid cell. A thin layer of 0.7% GG gel containing 2.5 mg/ml ALP was placed on a bottom liquid cell glass and kept in CaGP solution for 3 days. Subsequently, the gel was washed in deionized water and subsequently incubated in deionized water for 1 day. The spring constant and the resonant frequency were determined by thermal tuning. AC-mode AFM images were collected from flat parts of the surface. The sample was scanned with the PNP-TR cantilever. The driving amplitude for this scan was 300 mV with a setpoint of 25 mV. Higher oscillation amplitudes prevented the cantilever tip from sticking to the gel during slow scanning. However, higher amplitudes (above 500 mV) blurred the image due to sample perturbation by oscillating tip. Scans were collected with a low scanning rate (0.1 Hz) to minimize perturbation.

Images were saved in original non-flattened format and subsequently processed by Gwyddion software (flattening, lines correction).

2.9. Micromechanical properties

Force-distance curves of material with different levels of mineralization, as well as non-mineralized GG gel in water were obtained with an Asylum Research, MFP-3 atomic force microscope. Force curves were collected in contact mode with the AC240TS cantilever (Olympus, spring constant: 0.3 - 4.8 N/m). 40 x 40 points maps of nanoindentation curves were collected from a square area of 50 µm x 50 µm.

The maximum force applied onto the hydrogel surface in the elastic indentation was 15 nN for AC240TS-R3 cantilevers, which corresponded to 100 mV trigger point. In order to convert the cantilever deflection signal from millivolts (mV) to nm (force-indentation), the deflection sensitivity of the instrument, and so the sensitivity of the probe, was calculated from calibration measurements on mica substrate, assumed to be an infinitely rigid substrate (zero indentation). The spring constant and the resonant frequency were determined by thermal tuning according to the spring constant tutor in Igor 15.0 software. The elastic modulus (E) for all the collected maps was determined by fitting a Hertz mathematical model. For all measurements ν was assumed to be 0.5 [57].

2.10. Biological tests

Biphasic hydrogel slices obtained by cross section along to gradient direction were incubated in 24-well plates (Nunclon) at 37°C for 2 h in Dulbecco's Modified Eagle Medium (DMEM PAA, Austria) supplemented with 10% fetal bovine serum, 1% penicilin/streptomicin, 2 mM L-glutamine (PAA, Austria). 200 µl of osteoblast-like MG-63 cells (European Collection of Cell Cultures, Salisbury, UK) were seeded on each sample ($3x10^4$ cells) and allowed to sediment. After 10 min, 800 µl of medium was added and cultures were carried out for 4 and 8 days at 37 °C and 5% CO_2.

Cell viability and morphology were evaluated after 4 and 8 days of incubation using live/dead staining and fluorescence microscopy. Cell culture medium was removed from each well and replaced with 1 ml of the staining solution – 0.1% calcein AM and 0.1% propidium iodide (Sigma) in PBS. Cells were incubated in the dark for 20 min at room temperature. Fluorescence microscopy images were taken using an Axiovert 40 CFL with HXP 120 C metal halide illuminator (Zeiss, Germany).

The metabolic activity of the cells was tested using an MTS assay (CellTiter 96® Aqueous One Solution Cell Proliferation Assay, Promega). 4 samples for each of 2 groups were tested – one mineralized for 3 days and the second non-mineralized. The hydrogels were prepared as previously described and seeded with $8x10^4$ cells on each sample. Cells were cultured for 4 and 8 days in DMEM (supplemented with 10% foetal bovine serum, 1% penicilin/streptomicin, 2mM L-glutamine), at 37 °C

and 5% CO_2. The MTS test was performed after the samples to fresh plates. 500 μl of DMEM was added for each sample followed by the addition of 100 μl MTS reagent. Cells were incubated for 4 h at 37°C and 5% CO_2. The concentration of soluble formazan was measured by FLUOstar Omega Microplate Reader (BMG LABTECH) at 570 nm. The results were presented as averages of 4 samples with standard deviations. Statistical analysis was performed according to the ANOVA test combined with a post hoc Tukey-Kramer multiple comparisons test at $p<0.001$.

3. Results

3.1. Morphology

To obtain biphasic monolithic samples, the mineralization of GG was carried out in a way in which CaGP substrate was provided from the upper surface of a cylindrical hydrogel. The level of mineralization, measured by the percentage of dry mass, gradually increased over time for all samples (Fig. 2). The material was mineralized only from the side that was in contact with the CaGP substrate. The opposite side remained non-mineralized for all samples, with some small exceptions, little globular precipitates or flat, thin layers in a non-mineralized zone. Usually, the mineralized zone that was produced during the first day of mineralization was not progressing deeper into the hydrogel. Only the level of mineralization was increasing. This way of mineralization in every case produced a sharp transition between mineralized and non-mineralized zones. Most of the mineralization took place in the bulk of the hydrogel with few exceptions.

In the experiments, two different parameters of the hydrogel were tested: ALP concentration (from 0.1 to 5 mg/ml) and GG concentration (from 0.7 to 1.3%) (Fig. 2). The first had a much more substantial effect on the mineralization process and CaP formation. For the lowest ALP concentration (Fig. 2 (g), (h), (i)), mineralization was slower, the maximum level of mineralization was lower, but the mineralized zone was deeper (approximately 8 mm depth). The samples with the highest percentage of ALP (Fig. 2 (a),(b),(c)) were mineralized very strongly close to the top surface and the mineralization zone did not penetrate more than 2 mm into the material. For these samples, the level of CaP mineralization after 7 days was around 20%.

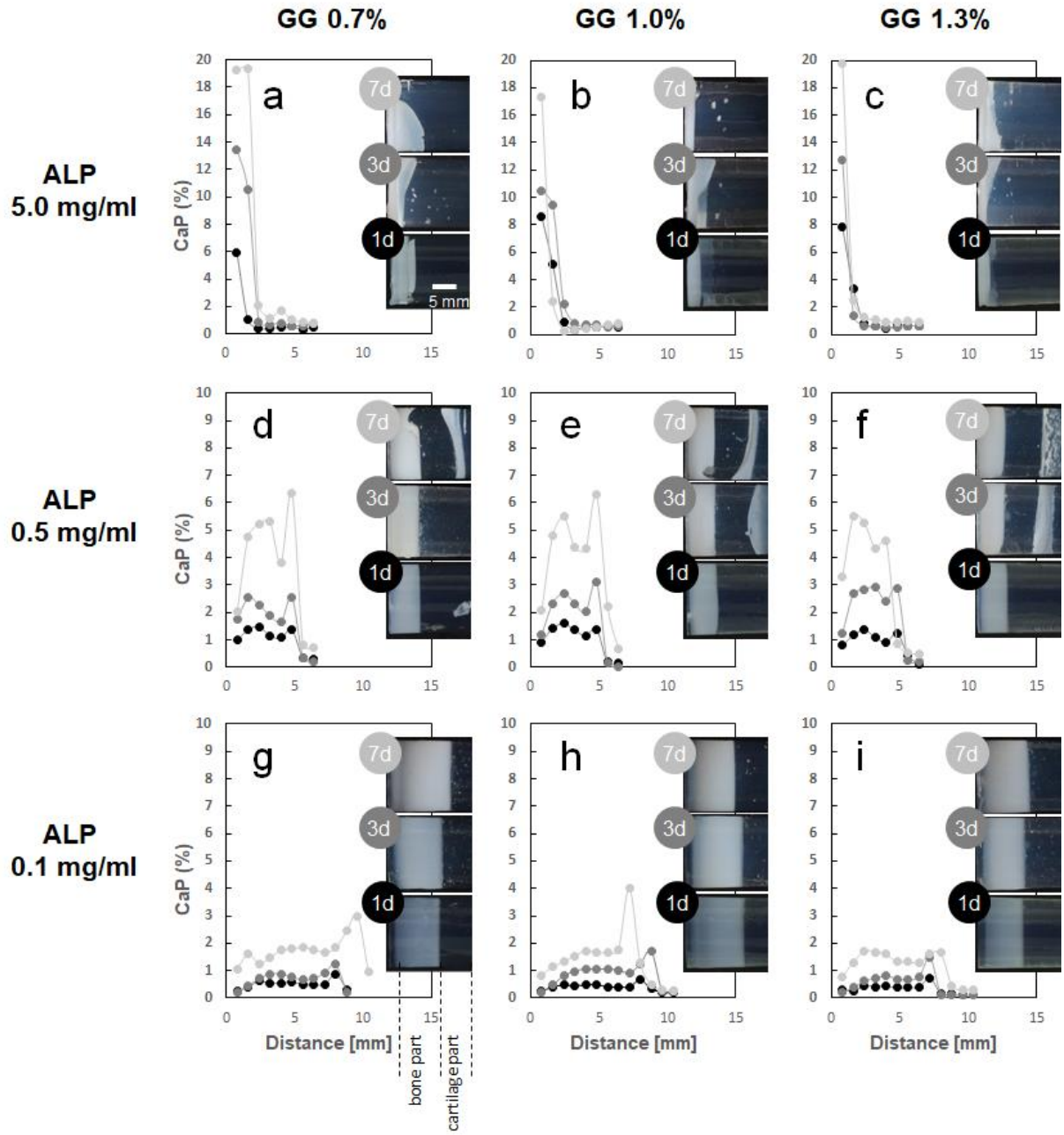

Fig. 2 CaP percentage profiles (left side) of biphasic GG hydrogels mineralized over 1 day (•, 1d), 3 days (•, 3d) and 7 days (•, 7d) and morphology of gradient samples used to create mineralization profile (right side). Left part of each picture shows white mineralized bone part, while left part shows transparent non-mineralized cartilage part as marked in (g). Three different concentrations of ALP were used: 5.0 mg/ml (a), (b), (c), 0.5 mg/ml (d), (e), (f) and 0.1 mg/ml (g), (h), (i). Three concentration of GG were used: 0.7% (a), (d), (g), 1.0% (b), (e), (h) and 1.3% (c), (f), (i). Scale bar marked in (a) equal to 5 mm is valid for all the pictures (a)-(i).

The intermediate level of mineralization (Fig. 2 (d),(e),(f)) was for ALP 0.5 mg/ml samples (around 5% after 7 days) and also the mineralization zone depth was between that noted for samples with 0.1 and 5 mg/ml ALP (5 mm depth). Samples with the lowest ALP concentration had the most uniform and homogeneous profile of mineralization: the interphase between two zones was straight, there was no mineralization outside, and no mineralization inside the non-mineralized zone. For 0.5 mg/ml ALP (Fig. 2 (d), (e), (f)) the mineralization profile was less uniform and thin mineralized surfaces

were present inside the non-mineralized zone after a longer mineralization time. However, in this case, no mineral deposits were present on the side surface of the hydrogel, which was the case for the 5 mg/ml ALP hydrogel (Fig. 2 (a),(b),(c)). For those samples, small mineralized globules were also present inside the non-mineralized zone. Part of a material closer to the top surface (between 0 and 2 mm) was poorly mineralized in the case of 0.5 and 0.1 mg/ml ALP samples (Fig. 2 (d)-(i)) and very strongly mineralized for 5 mg/ml ALP samples (Fig. 2 (a), (b), (c)).

The highest level of mineralization was reached close to the gel surface for 5 mg/ml ALP samples (Fig. 2 (a)-(c)) and close to the interface for 0.5 and 0.1 mg/ml ALP samples (Fig. 2 (d)-(i)). For the 0.1 mg/ml ALP sample, this phenomenon of an increased level of mineralization at the interface was much stronger than for the 0.5 mg/ml ALP sample and in some cases was twice that of the rest of the mineralized zone. Interestingly, this phenomenon was not present (or only to a small degree) in 1.3% GG samples (Fig. 2 (i)).

Differences between various concentrations of GG were mostly visible for GG containing 0.1 mg/ml ALP. In this case, there was a slight progression of the mineralization zone into the hydrogel over time for 0.7 and 1.3% GG and the opposite effect was observed for 1.0% GG. The second difference related to GG concentrations is the much higher level of mineralization at the interface for 0.7% and 1.0% GG, which was not that prominent for the 1.3% GG samples (Fig. 2 (f), (i)).

3.2. Chemical analysis

SEM and EDX analysis of the mineralized sample (0.7% GG + 0.5 mg/ml ALP) for 72 h revealed the presence of calcium and phosphorus in the mineralized part and only a small amount of these elements in the other part (Fig. 3 (b)-(d)). In the mineralized part there was a much higher signal from Ca and P than from carbon or oxygen. The Ca/P ratio for the mineralized part was close to 1.0. The EDX maps revealed a sharp transition between mineralized and non-mineralized zones in terms of Ca and P. The same sharp transition was recorded in Raman spectroscopy mapping (Fig. 4 (d)) corresponding to 963 cm^{-1} peak related to symmetric ν_1 PO_4^{3-} stretching in phosphate group. Another Raman shift at 1072 cm^{-1} (ν_3 asymmetric stretch) peak characteristic for crystalline hydroxyapatite was present, although it had a very small intensity. The presence of phosphate groups was also confirmed by FTIR spectroscopy for the mineralized part of the sample (Fig. 4 (f)). Peaks at 557 and 598 cm^{-1} were attributed to ν_4 vibration components of PO_4^{3-}. Peaks between 970-1100 cm^{-1} were attributed to the ν_1 and ν_3 stretching of PO_4^{3-} groups. These bands overlapped with the 1020 cm^{-1} band (Fig. 4 (e)) related to the stretching C-O vibration of GG [58].

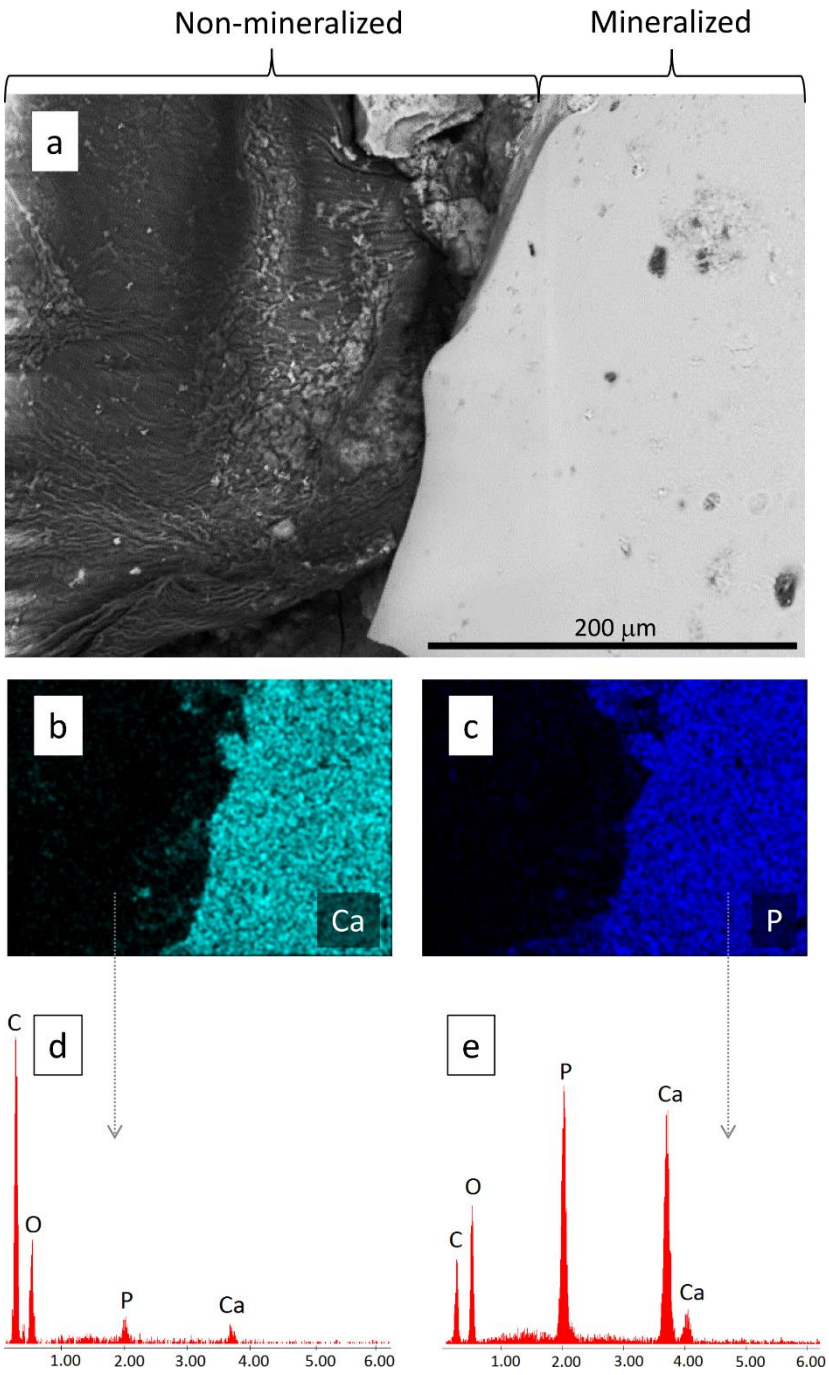

Fig. 3 SEM image of interface between mineralized (right) and non-mineralized (left) phase of biphasic GG sample (a), corresponding EDX maps of calcium (b) and phosphorus (c) and respective EDX spectra of calcium (d) and phosphorus (e). All samples after diffusion-limited mineralization in CaGP for 72 h.

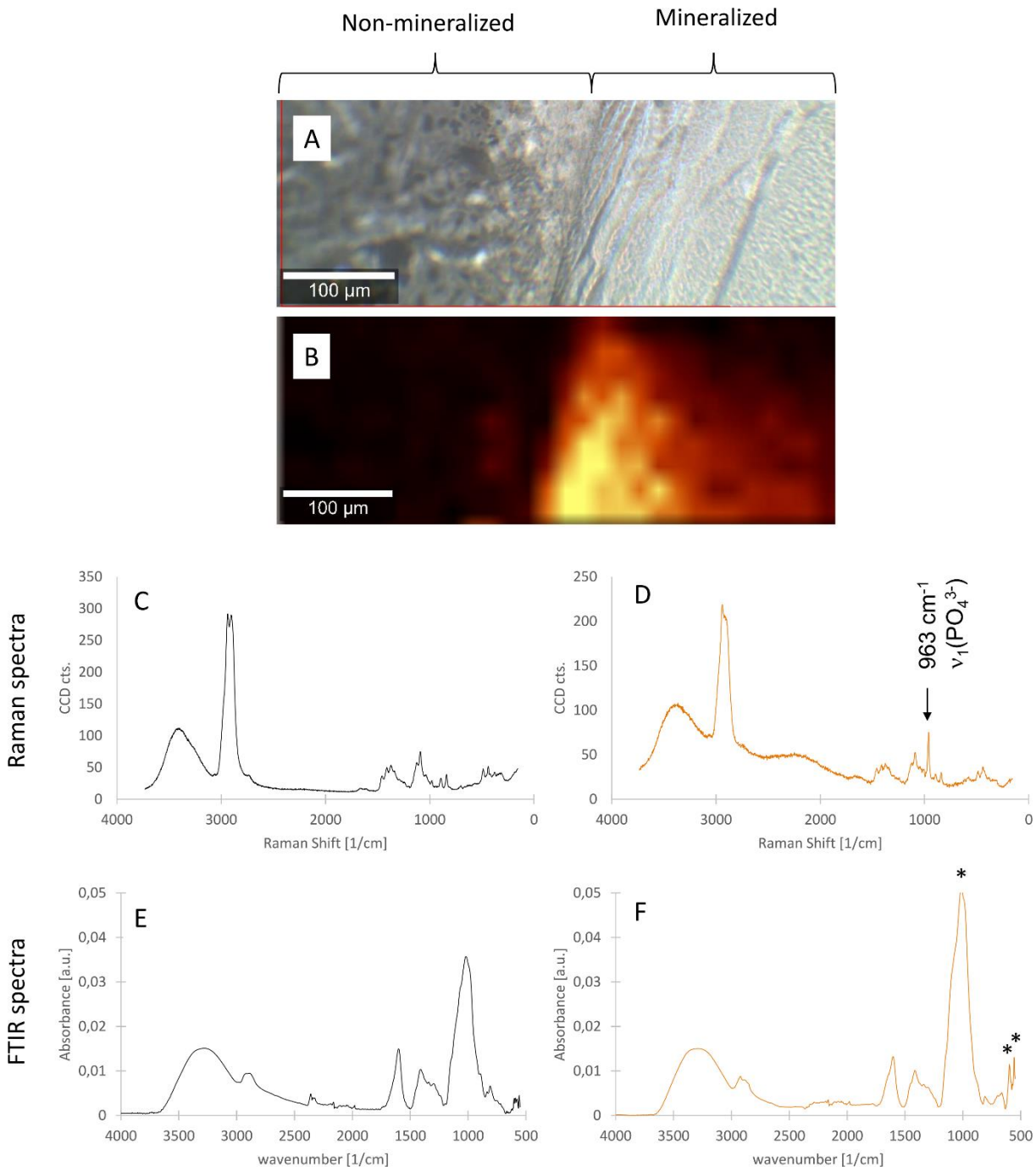

Fig. 4 Interface between mineralized (right) and non-mineralized (left) phase of biphasic GG sample (a, b). Confocal microscope image (a) and corresponding Raman map for the band at 963 cm^{-1} (b). Raman spectra of non-mineralized (c) and mineralized part (d) of GG biphasic sample. FTIR spectra of non-mineralized (e) and mineralized (g) part of GG biphasic sample. All samples after diffusion-limited mineralization in CaGP for 72 h.

3.3. Microstructure

The freeze dried non-mineralized GG was smooth (Fig. 5 (a)), while those mineralized for 72 h in CaGP showed mineral deposits that formed small globules with pores between them (Fig. 5 (b)). The white colour in the SEM image in BSD mode shows the presence of elements with higher atomic mass, such as calcium and potassium. The distribution of mineral deposits was not uniform. There were places with a more condensed and looser structure.

AFM images collected in the wet state under water showed a smooth surface for the non-mineralized sample (Fig. 5 (c)) and the presence of globules and pores in the mineralized sample (Fig. 5 (d)). Mineralized GG was rough (Ra = 33.6 $\pm$ 2.7 nm, RMS = 349 $\pm$ 22 nm) as compared to more wavy and smooth non-mineralized GG (Ra = 3.9 $\pm$ 1.1 nm, RMS = 141 $\pm$ 61 nm). The size of the globules was estimated to be around 500 nm. Higher magnification AFM images of GG samples in a dried state after mineralization (Fig. 5 (f)) showed the internal structure of globules made of even smaller features, probably mineral nanocrystals visible as small dots, 10-20 nm in diameter. The non-mineralized GG after drying looked similar, it was also rough but much more uniform and without nanocrystals visible (Fig. 5 (e)).

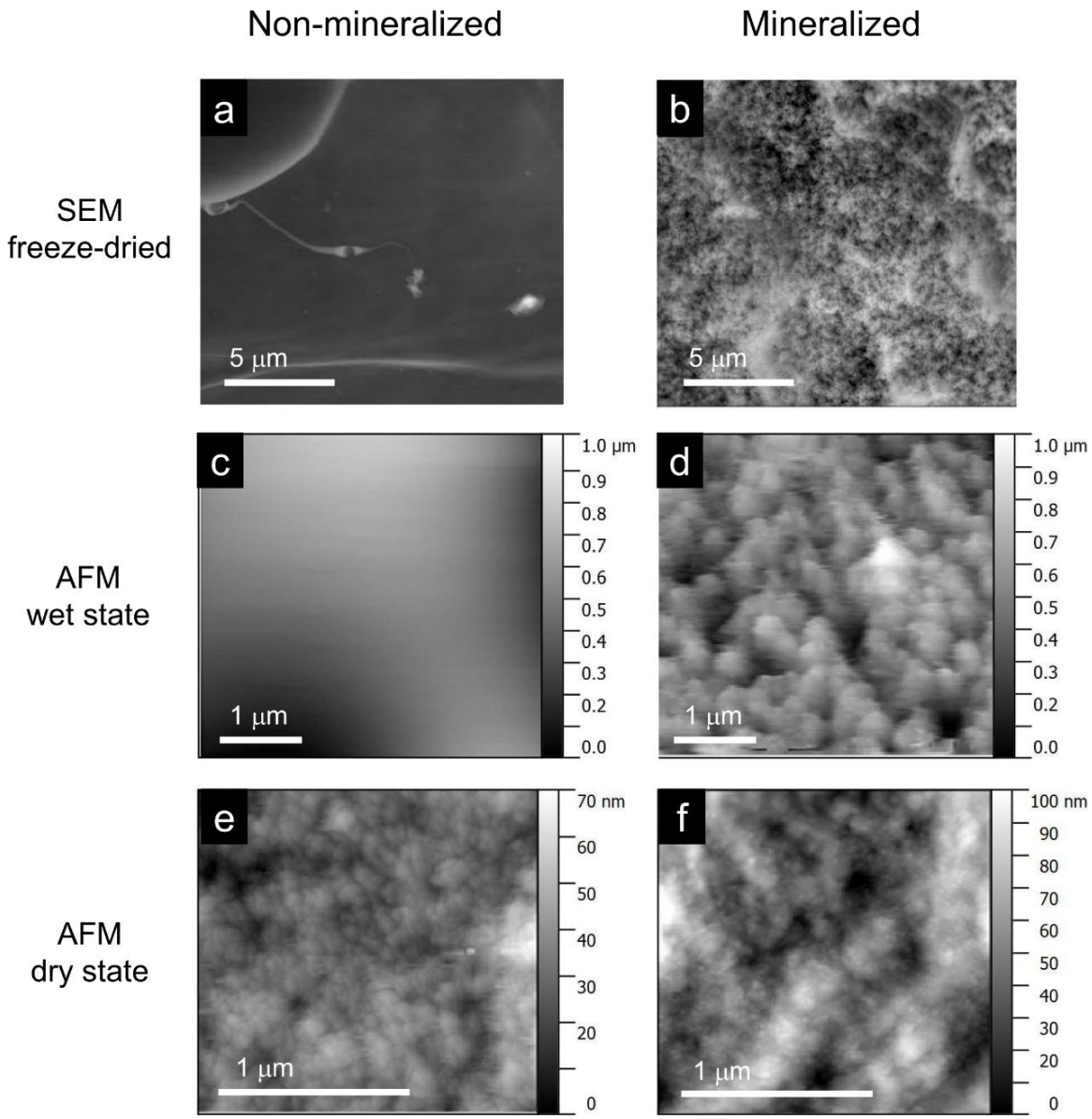

Fig. 5 SEM images in BSD mode (a, b) and AFM (c, d, e, f) images of GG microstructure: non-mineralized (a, c, e) and after 72 h mineralization in CaGP (b, d, f). AFM on samples in water (c, d) and in dry state (e, f).

3.4. Mechanical properties

The mechanical properties of mineralized and non-mineralized GG studied by AFM, compression test, and rheology are shown in Fig. 6. The stiffness map for non-mineralized GG (Fig. 6 (a)) was uniform with only low Young's modulus values (median 17.8 kPa). The stiffness map for mineralized GG (Fig. 5 (b)) was less uniform with places with a high (500 kPa) Young's modulus and places with a low (<20 kPa) E value that formed holes between the more rigid regions. The distribution of E values (Fig. 6 (c),(d)) was very narrow for non-mineralized GG and spread to higher values after mineralization, achieving a median value of 206.5 kPa.

The bulk stiffness measurement of 0.7% GG containing 0.5 mg/ml ALP in compressive test showed a 20-fold increase in the E modules after 72 h of mineralization. The storage modulus (G') increased an order of magnitude during mineralization and the loss modulus (G'') increased more than two orders of magnitude (Fig. 6 (e), (f)).

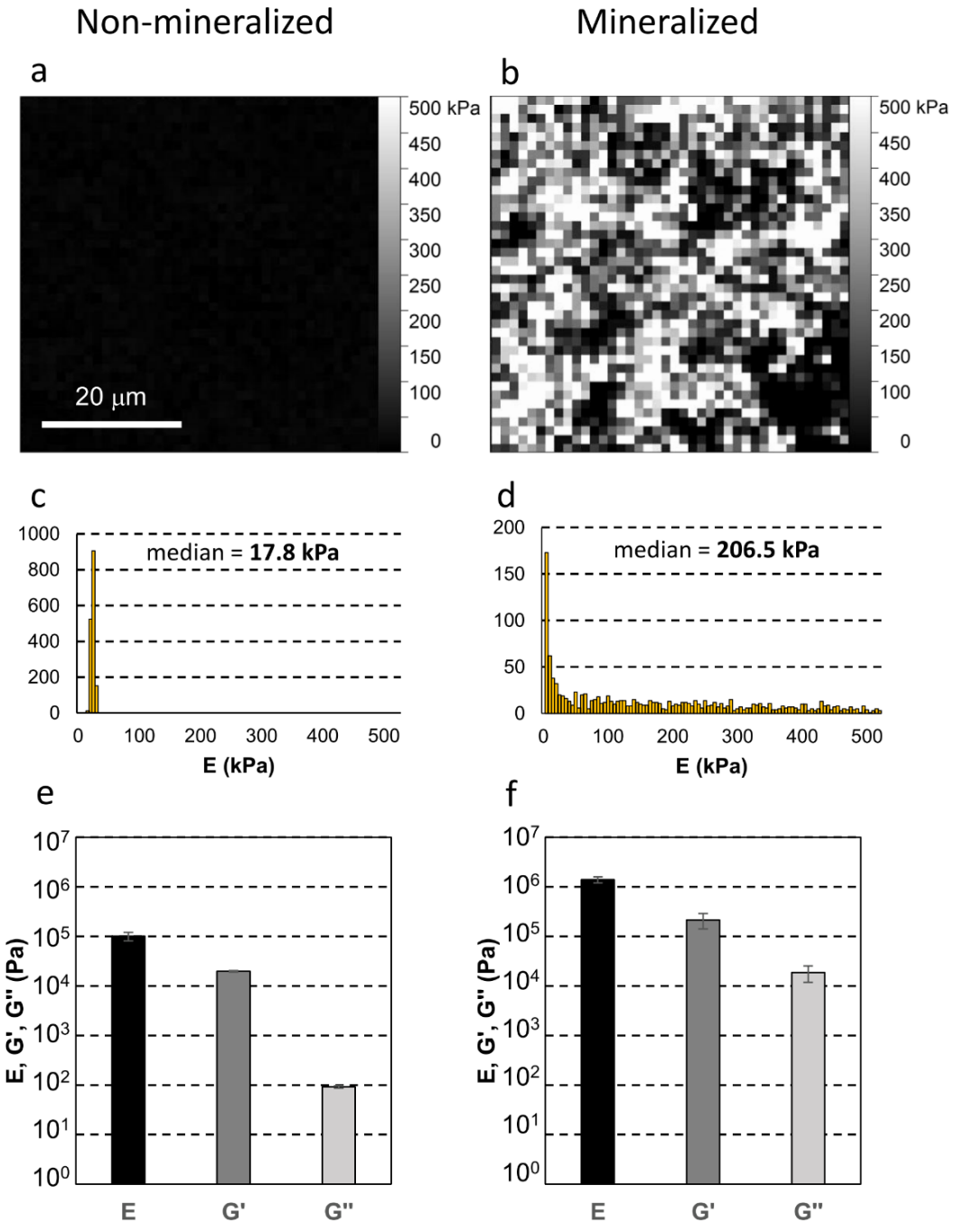

Fig. 6 Young's modulus maps for 0.7% GG containing 0.5 mg/ml ALP before (a) and after mineralization (b) in aqueous environment measured by AFM (a, b) and corresponding Young's modulus distribution diagrams (c, d). Bulk Young's modulus studied by Zwick, storage (G') and loss modulus (G'') studied by rheology before (e) and after 72 h mineralization (f). Error bars show standard deviation.

3.5. Biological response

The behaviour of MG-63 cells on non-mineralized, mineralized, and biphasic GG samples is shown in Fig. 7. After 8 days of culture, cells were grown on non-mineralized GG in the form of agglomerates. Cells were mostly round, poorly spread, and their number was low (Fig. 7 (a)). On mineralized material (Fig. 7 (b)) almost the entire surface was covered by cells. Live/dead staining showed very little number of dead cells on both materials (less than 2%). Cell viability, as studied by the MTS test, was almost ten times higher on mineralized samples than on non-mineralized samples (Fig. 7 (c)). Cells on mineralized GG had higher viability than those cultured on non-mineralized GG. Cell viability on non-mineralized material increased between day 4 and day 8, however, there was no increase in viability for cells growing on mineralized GG in the same period of time.

MG-63 cells were also cultured in 0.7% GG subjected to gradient mineralization for 8 days (Fig. 7 (d), (e)). Almost all cells were growing on the mineralized side, they were well spread and elongated, with morphology compared to that on the mineralized sample (Fig. 7 (b)). The non-mineralized part remained almost completely empty except for one small cell agglomerate close to the interface non-mineralized/mineralized zone.

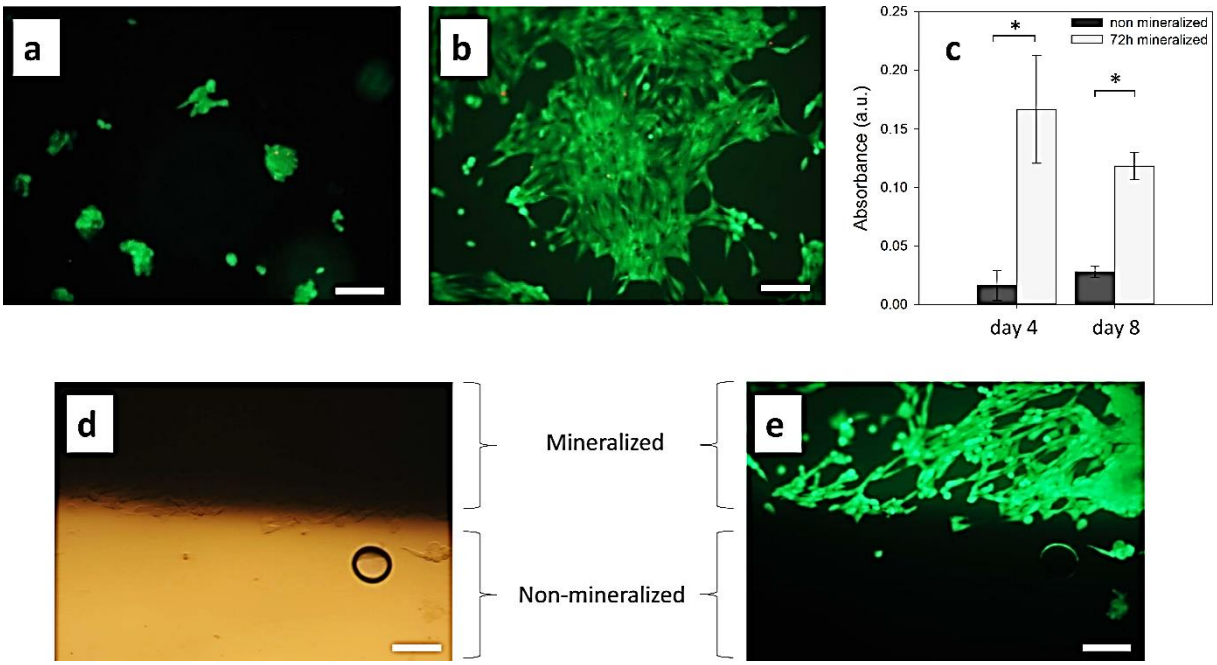

Fig. 7 Fluorescent images after live/dead staining of MG-63 cells cultured on 0.7% GG (a) and mineralized 0.7% GG for 8 days (b). MTS test for cells cultured on those materials (c), *$p < 0.001$, error bars show standard deviation. Morphology of MG-63 cells cultured at the interface non-mineralized/mineralized zone (d, e); optical microphotography (d), fluorescent microscopy after live/dead staining (e), white bar = 100 μm.

4. Discussion

4.1. Mineralization profile

The primary objective of this research was to develop a method that can selectively alter one part of the hydrogel material by producing a mineral content and stiffness that is considered favourable in regeneration of osteochondral region regeneration as it can closely resemble naturally occurring gradients [15]. Because of the diffusion-limited enzymatic mineralization method developed in this study, it was possible to produce a biphasic monolithic hydrogel scaffold in which only one part was mineralized, while the other remained unaltered. The mineralization profile was not influenced by the concentration of GG, but was mainly dependent on the concentration of ALP and the duration of the mineralization process.

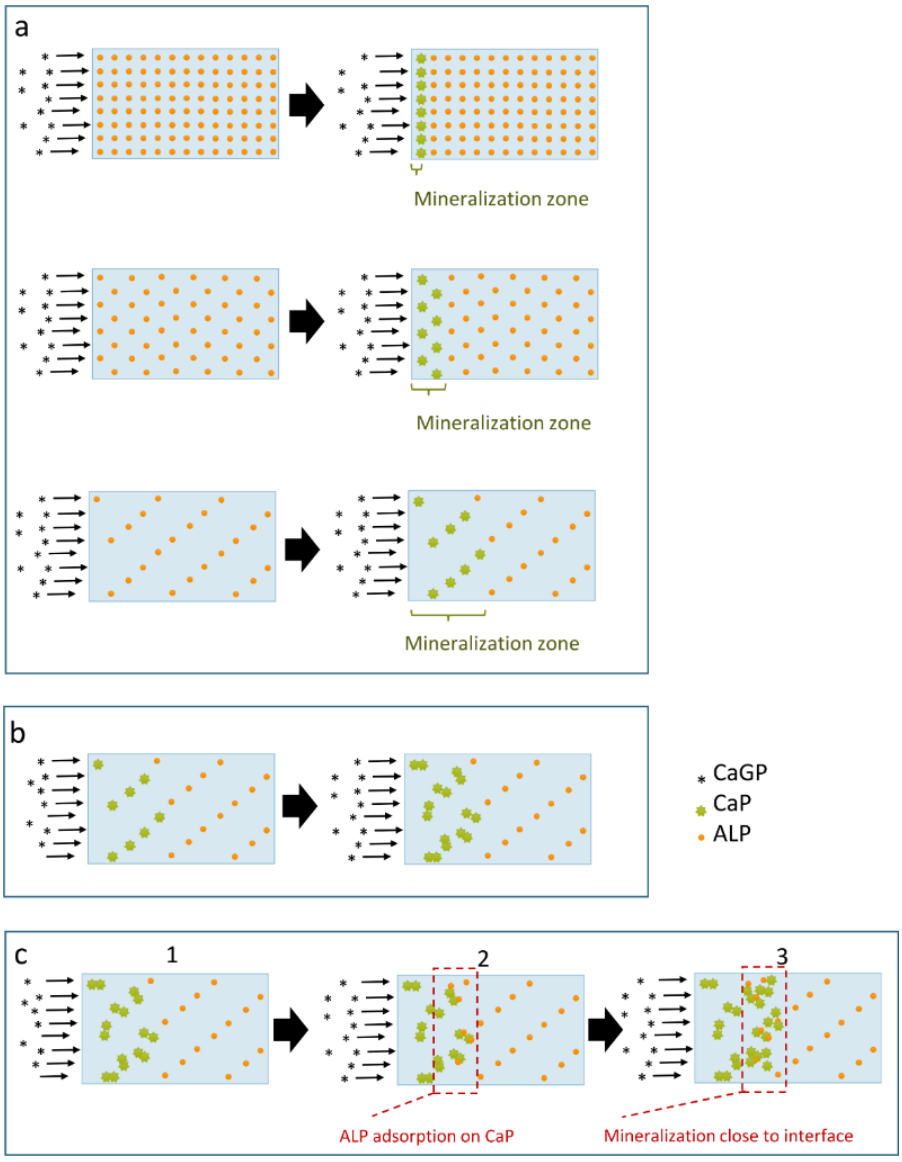

Fig. 8. Hypothetical formation of mineralization profiles in GG hydrogels. Depth of mineralization zone is strongly dependent on ALP concentration. Slower reaction due to lower ALP concentration allows for deeper CaGP diffusion (a). Mineral precipitates formed in mineralization zone act as further nucleation sites thus mineralization zone depth is not changing over time but CaP concentration increases (b). Adsorption of ALP on mineral deposits at the interface and acceleration of mineralization process on that region as a result CaP concentration increases (c).

A higher concentration of ALP, i.e., 5 mg/ml (see Fig. 2 (a-c)), resulted in an increased mineralization rate and produced a higher amount of CaP mineral, but the depth of mineralization was lower. In this case, CaGP diffusion was hindered, presumably because of a large amount of CaP precipitates. Furthermore, the CaGP substrate was consumed more rapidly by ALP present at high concentration before it could reach deeper parts of the hydrogel. The mineral formation for these types of samples is shown in Fig. 8 (a), line 1.

The blockage of diffusion might also be responsible for much deeper side surface mineralization of these samples (inorganic phosphate from CaGP was released close to the surface in this case). For lower concentrations of ALP, that is, 0.5 and 0.1 mg/ml (see Fig. 2 (d)-(i)), the enzymatic reaction was slower and the substrate was able to diffuse much deeper (Fig. 8 (a), lines 2 and 3). This effect of superficial mineralization, where the process is mostly limited to a few millimetres in depth and bulk of a material remains unchanged, was already presented in other studies where mineralization by urease was used [59] or where hydrogels were mineralized by alternate soaking [60]. The diffusion of molecules in hydrogels is related to the size of the mesh [61]. After CaP precipitation, the effective mesh size of the hydrogel might be lower and therefore the diffusion rate is decreasing. However, it is unclear if in this case the mineral part is closely connected to GG chains and makes it thicker, therefore decreasing the mesh size. The nanometer-sized particles located inside hydrogel pores are probably blocking diffusion and due to extensive surface area, may also be responsible for ALP adsorption. Douglas et al. showed that CaP particles inside the GG hydrogel can be as small as 15 nm [56].

An interesting fact is that the mineralization depth after one day was stable and was not progressing over time inside the hydrogel (except for 0.1 mg/ml of ALP). Only the level of mineralization was increasing. This was probably because the precipitates previously produced acted as nucleation sites for the new ones. The mineral formation for this type of sample is shown in Fig. 8 (b).

It is probable that other types of nucleation site were responsible for unusual precipitation on CaP inside the non-mineralized zone. In this case, the majority of CaP precipitated in the already mineralized part, but a small amount of ions at concentration below equilibrium solubility diffused deeper and presumably precipitated in small air bubbles or cracks inside the hydrogel (the solubility for dicalcium phosphate at pH = 7 is 4.8×10^{-2} g/dm^3 and for hydroxyapatite 3×10^{-4} g/dm^3) [62].

Additionally, the interface between the two phases also acted as a preferred site of nucleation for low-concentration ions in that region. ALP diffusing from deeper parts might be adsorbed on already precipitated CaP phases close to the interface, further accelerating its mineralization (Fig. 8 (c)). This is why the level of mineralization was much higher at the interface and also why this phenomenon was more prominent at later stages of the mineralization process. A similar phenomenon was observed when the thin layers of hydrogel were mineralized under a glass slide (Supplementary Figure 2).

Therefore, because of this unexpected phenomenon, not in every condition a gradient mineralization profile was possible. Blocking the diffusion caused the formation of an undesirable sharp transition, which is not preferable as the osteochondral junction. A sharp transition was also present in many cases inside the hydrogel close to the interface zone as this part was unexpectedly mineralized to a greater extent. Experimental data showed that the first effect can be reduced by lowering the concentration of ALP to 0.5 mg/ml. The second effect can be reduced by: (1) using a higher concentration of ALP , (2) increasing the concentration of GG, and (3) decreasing the process time. A sharp transition is also visible for samples prepared for SEM and Raman imaging (Fig. 3 and 4). In this case, the resulted transition was mostly related to the difference in water content between the mineralized and non-mineralized part. The shrinkage of the high amount of water containing nonmineralized part during sample preparation caused sample deformation, emphasizing the effect of a sharp transition. However, even on these images traces of mildly mineralized material close to the transition zone are visible.

Poor mineralization close to the top surface was observed for 0.1 mg/ml ALP samples and to a lesser extent for 0.5 mg/ml ALP samples. It was more likely related to rapid ALP diffusion from hydrogels. ALP can diffuse outside freely and was previously demonstrated that for 0.7% GG samples with 8 mm diameter and 4 mm thickness, 40% of the enzyme was released in 270 min [51]. A similar phenomenon has already been reported in our previous research [63]. For small cylindrical samples with low concentrations of ALP, mineralization mostly takes place inside the hydrogel as a result of the loss of ALP from the surface. Faster mineralization rates at the beginning for highly concentrated ALP samples must have prevented ALP depletion in further stages of mineralization.

0.7% GG samples with 0.5 mg/ml ALP mineralized for 3 days were further investigated as an example of intermediate mineralization level and relatively uniform mineralization profile. This sample composition was also investigated in our previous work [56,64]. For these samples, the mineralization level close to the surface was only slightly lower than in the rest of the volume, and there were also no CaP precipitates in the non-mineralized zone.

4.2. Modification of material properties and cell response

The goal of this study was to obtain distinctly chemically and mechanically different areas in one material: mineralized for bone and non-mineralized for cartilage. The non-mineralized part of the material remained unchanged. The mineralization of the bone-like part was achieved by diffusion-limited enzymatic mineralization. The formation of CaP inside the GG hydrogel was shown directly by EDX, FTIR, and Raman spectroscopy/imaging and indirectly by the increase in the dry mass percentage. The SEM and AFM images in dry state showed that the CaP crystals formed by this method were smaller than 1 µm. Evidence of the formation of apatite nanocrystals (15 nm in diameter) achieved by this method was demonstrated by Douglas et al. using XRD and TEM [56].

The AFM and SEM images of the mineralized hydrogel showed a rough surface with a globular structure and pores of less than 1 µm. This globular mineralization pattern was not the effect of freeze-drying because it was also visible for GG hydrogels in their native wet state (see Fig. 5 (c) (d)). Observed globules may arise from the inhomogeneity of the GG hydrogel at the nanoscale, which was also shown in this study. In our AFM measurement setup, resolution was too low to observe separated GG helices with thickness approximately 1 nm [65] and CaP crystals of 15 nm, therefore it is also not clear whether CaP particles are closely associated with GG or separated.

The stiffness distribution of the mineralized surface showed various values of Young's modulus, ranging from very low (< 1 kPa) to high (> 500 kPa). The E values for the mineralized hydrogel were characterized by an exponential distribution, while the non-mineralized material was characterized by a normal distribution. This would imply that non-mineralized material was homogenous at the micrometer scale range, while the mineralized exhibited a wide range of distinct E values depending on the level of mineralization in a particular place and also in the nearest surrounding. The median E value for the mineralized surface was more than 10 times higher than for the non-mineralized one. This increase was consistent with the bulk stiffness measurements of G' obtained by rheometry and E in the compression test. Two distinct zones of different stiffness obtained by the proposed method were expected to have a significant impact on cell differentiation into the bone or cartilage linage. As it was shown before, MSC differentiate into osteoblasts within the 62 to 68 kPa range [66] and chondrogenic differentiation of MSCs is promoted by soft substrates (0.5 kPa) [67].

Enzymatic mineralization of the GG hydrogel led to superior cell adhesion, as demonstrated by live/dead staining. In the first experiment (see Fig. 7 (a), (b), (c)) after day 4 almost the entire surface was covered by MG-63 cells; therefore, there was no further increase in viability after 8 days. Slight decrease in cell viability may be attributed to decreased metabolic activity after 8 days, which may be

characteristic for non-proliferating MG-63 cells, due to the lack of free surface for cells to adhere. For non-mineralized material, cells were growing mostly in clusters, which was caused by their poor adhesion to this substrate. Although chondrocytes were not tested, the morphology of MG-63 cells in this case was more similar to that characteristic of cartilage tissue [68]. In the second experiment (see Fig. 7 (d), (e)) cells seeded in the interface area were spreading and proliferating merely on the mineralized zone. It was presumably due to higher stiffness, higher roughness, and higher surface area as shown by others [54]. This was clearly demonstrated that by this kind of mineralization, material of two distinct zones can be obtained and that the chemical and mechanical properties at the interface act as strong signals for cells to attach, spread, and proliferate. This kind of sharp transition is considered beneficial characteristics in the case of osteochondral defect regeneration, where cell differentiation in two distinct lineages is desirable in a very close region (< 5 μm) [69].

Structural and mechanical differences alone are prerequisites to establish an effective transition between two different tissues, but the establishment of biochemical gradients, particularly in the interface region is also needed [70]. Therefore, further research is required. This biochemical gradient can be achieved by incorporating growth factors such as bone morphogenetic proteins (BMP) and nanoparticles loaded with transforming growth factor alpha (TGFα). Mineral nanocrystals can also act as a high surface absorber of growth factors [53].

4.3. Perspectives of enzymatic mineralization limited by diffusion

The monolithic hydrogel scaffold obtained by the limited substrate diffusion enzymatic mineralization method is a valuable alternative to achieve a mineral gradient inside the hydrogel material. It does not require the introduction of ceramic powder to the hydrogel prior to gelation, which may generate additional problems with agglomeration, sedimentation, inhomogeneous distribution, and the lowering of the mechanical strength of the scaffold. The method can potentially be adapted to other materials, as it is based on enzymatic mineralization that works in other biopolymers – fibrin, silk, whey protein isolate [55,71,72] to obtain material with better biological response and strength needed for osteochondral applications. The potential limiting factor of the presented method may be the depth of mineralized zone. However, in our experiments, depth of around 10 mm was achieved (however, only for low ALP concentration), therefore, in this case the obtained bone part is similar in size to existing commercial products [73].

Hydrogel osteochondral scaffolds produced by our method are intended to be used as a cell-free approach, which is increasingly popular as a more simple and reliable and low cost solution [6]. The presence of cells in the osteochondral scaffold is still debatable. The cell-free approach can

eliminate the need for cell source and legislative concerns [7]. Instead, cells may be recruited to scaffolds from surrounding tissues, as recently demonstrated with a hydrogel scaffold containing specific MSC recruiting aptamers [32] or affinity peptide sequences [35]. A similar acellular GG scaffold with mineralized alginate by the addition of HAP powder was successfully used to regenerate critical osteochondral defects in rabbits [34]. The large surface area of nanometric CaP particles inside the hydrogel can be potentially used to absorb bone specific molecules, thus creating not only CaP, but also other chemical gradients similarly to those present in osteochondral region [15].

In our method, the mineralization gradient profile and the stiffness of the material stiffness can be relatively easily by changing the ALP concentration and the time of the process. Therefore, the stiffness of the material can be adapted to chondrocyte and osteoblasts, or its adapted stiffness can induce differentiation of the MSC differentiation into chondritic or osteogenic linage [66,67]. The hydrogel scaffold should also provide the exchange of chemical signals between two layers necessary to facilitate a proper regeneration process [74]. From this perspective, a sharp transition on the interface obtained under many tested conditions is not preferable, as it indicates that diffusion of the low molecular substrate (CaGP) might have been blocked. The hydrogel structure after mineralization should still ensure diffusion of the necessary molecules. Therefore, a lower mineralization level and a more uniform gradient transition are preferable in this case.

Due to the simplicity of the proposed method, in the authors' opinion, it can be adapted to microfluidic devices to produce the organ-on-chip model of the osteochondral junction. First, the mineralization process can be conducted in a microfluidic cell in more controlled manner by providing the appropriate amount of CaGP substrate by microfluidics and due to the optical transparency of GG hydrogel. After the mineralization process, the gradient material can be seeded with cells and cultured owing to the architecture of the microfluidic chamber under two different conditions, i.e., dedicated to bone and cartilage parts. A similar idea of a dual-flow bioreactor that simulates the osteochondral junction has recently been explored [75].

This research presents a new approach to obtain a partially mineralized hydrogel with the use of enzymatic mineralization by limiting substrate diffusion. The scope of this research was to confirm the feasibility of mineral gradient formation and the positive relation between material stiffness and basic cell response. Therefore, the question of how the material obtained will act within the osteochondral defect is still open. More in-depth biological research that involves the differentiation of MSC and its characterisation by tissue-specific markers for bone and cartilage should provide a justification for our approach.

5. Conclusion

The substrate diffusion-limiting method for the enzymatic mineralization of GG proposed in this study allowed for the successful fabrication of biphasic monolithic GG hydrogels. Such hydrogels consist of the two phases: non-mineralized and mineralized. Parameters of the mineralization profile, such as depth and CaP content, were adjusted by ALP concentration, duration of the process, but less by GG concentration. The method was able to produce monolithic biphasic material with two zones with different chemical compositions, microstructures, and mechanical properties that were responsible for the specific biological response.

Acknowledgments

K.P. acknowledges European Society for Biomaterials for Racquel LeGeros Award, and FSS mobility program which supported his stay at ERRMECe Laboratory, University of Cergy-Pontoise, France and at Department of Biomaterials University of Oslo, Norway, respectively. This study was supported by the National Science Centre Poland (No 2018/29/N/ST8/01544) and by the program ”Excellence Initiative–Research University” for AGH University of Science and Technology, Kraków, Poland.

References

[1] Deng C, Chang J, Wu C. Bioactive scaffolds for osteochondral regeneration. J Orthop Transl 2019;17:15–25. https://doi.org/10.1016/j.jot.2018.11.006.
[2] Meng X, Ziadlou R, Grad S, Alini M, Wen C, Lai Y, et al. Animal Models of Osteochondral Defect for Testing Biomaterials. Biochem Res Int 2020;2020:1–12. https://doi.org/10.1155/2020/9659412.
[3] DeFroda SF, Bokshan SL, Yang DS, Daniels AH, Owens BD. Trends in the Surgical Treatment of Articular Cartilage Lesions in the United States from 2007 to 2016. J Knee Surg 2021;34:1609–16. https://doi.org/10.1055/s-0040-1712946.
[4] Frassica MT, Grunlan MA. Perspectives on Synthetic Materials to Guide Tissue Regeneration for Osteochondral Defect Repair. ACS Biomater Sci Eng 2020;6:4324–36. https://doi.org/10.1021/acsbiomaterials.0c00753.
[5] Panseri S, Russo A, Cunha C, Bondi A, Di Martino A, Patella S, et al. Osteochondral tissue engineering approaches for articular cartilage and subchondral bone regeneration. Knee Surg Sports Traumatol Arthrosc 2012;20:1182–91. https://doi.org/10.1007/s00167-011-1655-1.
[6] Boffa A, Solaro L, Poggi A, Andriolo L, Reale D, Di Martino A. Multi-layer cell-free scaffolds for osteochondral defects of the knee: a systematic review and meta-analysis of clinical evidence. J Exp Orthop 2021;8:56. https://doi.org/10.1186/s40634-021-00377-4.

[7] Ai C, Lee YHD, Tan XH, Tan SHS, Hui JHP, Goh JC-H. Osteochondral tissue engineering: Perspectives for clinical application and preclinical development. J Orthop Transl 2021;30:93–102. https://doi.org/10.1016/j.jot.2021.07.008.
[8] Zhang X, Liu Y, Zuo Q, Wang Q, Li Z, Yan K, et al. 3D Bioprinting of Biomimetic Bilayered Scaffold Consisting of Decellularized Extracellular Matrix and Silk Fibroin for Osteochondral Repair. Int J Bioprinting 2021;7:401. https://doi.org/10.18063/ijb.v7i4.401.
[9] Duan P, Pan Z, Cao L, Gao J, Yao H, Liu X, et al. Restoration of osteochondral defects by implanting bilayered poly(lactide-co-glycolide) porous scaffolds in rabbit joints for 12 and 24 weeks. J Orthop Transl 2019;19:68–80. https://doi.org/10.1016/j.jot.2019.04.006.
[10] Yang T, Tamaddon M, Jiang L, Wang J, Liu Z, Liu Z, et al. Bilayered scaffold with 3D printed stiff subchondral bony compartment to provide constant mechanical support for long-term cartilage regeneration. J Orthop Transl 2021;30:112–21. https://doi.org/10.1016/j.jot.2021.09.001.
[11] Peters AE, Akhtar R, Comerford EJ, Bates KT. The effect of ageing and osteoarthritis on the mechanical properties of cartilage and bone in the human knee joint. Sci Rep 2018;8:5931. https://doi.org/10.1038/s41598-018-24258-6.
[12] Trinity Centre for Bioengineering, Department of Mechanical Engineering, Parsons Building, Trinity College Dublin, Dublin 2, Ireland, Gannon A, Nagel T, Bell A, Avery N, Kelly D. Postnatal changes to the mechanical properties of articular cartilage are driven by the evolution of its collagen network. Eur Cell Mater 2015;29:105–23. https://doi.org/10.22203/eCM.v029a09.
[13] Antons J, Marascio MGM, Nohava J, Martin R, Applegate LA, Bourban PE, et al. Zone-dependent mechanical properties of human articular cartilage obtained by indentation measurements. J Mater Sci Mater Med 2018;29:57. https://doi.org/10.1007/s10856-018-6066-0.
[14] Nooeaid P, Salih V, Beier JP, Boccaccini AR. Osteochondral tissue engineering: scaffolds, stem cells and applications. J Cell Mol Med 2012;16:2247–70. https://doi.org/10.1111/j.1582-4934.2012.01571.x.
[15] Fu J-N, Wang X, Yang M, Chen Y-R, Zhang J-Y, Deng R-H, et al. Scaffold-Based Tissue Engineering Strategies for Osteochondral Repair. Front Bioeng Biotechnol 2022;9:812383. https://doi.org/10.3389/fbioe.2021.812383.
[16] Wei W, Dai H. Articular cartilage and osteochondral tissue engineering techniques: Recent advances and challenges. Bioact Mater 2021;6:4830–55. https://doi.org/10.1016/j.bioactmat.2021.05.011.
[17] Lin T-H, Wang H-C, Cheng W-H, Hsu H-C, Yeh M-L. Osteochondral Tissue Regeneration Using a Tyramine-Modified Bilayered PLGA Scaffold Combined with Articular Chondrocytes in a Porcine Model. Int J Mol Sci 2019;20:326. https://doi.org/10.3390/ijms20020326.
[18] Chicatun F, Rezabeigi E, Muja N, Kaartinen MT, McKee MD, Nazhat SN. A bilayered dense collagen/chitosan hydrogel to model the osteochondral interface. Emergent Mater 2019;2:245–62. https://doi.org/10.1007/s42247-019-00044-6.
[19] Liang X, Duan P, Gao J, Guo R, Qu Z, Li X, et al. Bilayered PLGA/PLGA-HAp Composite Scaffold for Osteochondral Tissue Engineering and Tissue Regeneration. ACS Biomater Sci Eng 2018;4:3506–21. https://doi.org/10.1021/acsbiomaterials.8b00552.
[20] Zhang W, Lian Q, Li D, Wang K, Hao D, Bian W, et al. The effect of interface microstructure on interfacial shear strength for osteochondral scaffolds based on biomimetic design and 3D printing. Mater Sci Eng C 2015;46:10–5. https://doi.org/10.1016/j.msec.2014.09.042.
[21] Asensio G, Benito-Garzón L, Ramírez-Jiménez RA, Guadilla Y, Gonzalez-Rubio J, Abradelo C, et al. Biomimetic Gradient Scaffolds Containing Hyaluronic Acid and Sr/Zn Folates for Osteochondral Tissue Engineering. Polymers 2021;14:12. https://doi.org/10.3390/polym14010012.
[22] Catoira MC, Fusaro L, Di Francesco D, Ramella M, Boccafoschi F. Overview of natural hydrogels for regenerative medicine applications. J Mater Sci Mater Med 2019;30:115. https://doi.org/10.1007/s10856-019-6318-7.
[23] Ng JY, Obuobi S, Chua ML, Zhang C, Hong S, Kumar Y, et al. Biomimicry of microbial polysaccharide hydrogels for tissue engineering and regenerative medicine – A review. Carbohydr Polym 2020;241:116345. https://doi.org/10.1016/j.carbpol.2020.116345.

[24] Hoffman AS. Hydrogels for biomedical applications. Adv Drug Deliv Rev 2012;64:18–23. https://doi.org/10.1016/j.addr.2012.09.010.
[25] Ullah F, Othman MBH, Javed F, Ahmad Z, Akil HMd. Classification, processing and application of hydrogels: A review. Mater Sci Eng C 2015;57:414–33. https://doi.org/10.1016/j.msec.2015.07.053.
[26] Chamkouri H. A Review of Hydrogels, Their Properties and Applications in Medicine. Am J Biomed Sci Res 2021;11:485–93. https://doi.org/10.34297/AJBSR.2021.11.001682.
[27] Correa S, Grosskopf AK, Lopez Hernandez H, Chan D, Yu AC, Stapleton LM, et al. Translational Applications of Hydrogels. Chem Rev 2021;121:11385–457. https://doi.org/10.1021/acs.chemrev.0c01177.
[28] Wei W, Ma Y, Yao X, Zhou W, Wang X, Li C, et al. Advanced hydrogels for the repair of cartilage defects and regeneration. Bioact Mater 2021;6:998–1011. https://doi.org/10.1016/j.bioactmat.2020.09.030.
[29] Lin H, Yin C, Mo A, Hong G. Applications of Hydrogel with Special Physical Properties in Bone and Cartilage Regeneration. Materials 2021;14:235. https://doi.org/10.3390/ma14010235.
[30] Xin W, Gao Y, Yue B. Recent Advances in Multifunctional Hydrogels for the Treatment of Osteomyelitis. Front Bioeng Biotechnol 2022;10:865250. https://doi.org/10.3389/fbioe.2022.865250.
[31] Chen Z, Xiao H, Zhang H, Xin Q, Zhang H, Liu H, et al. Heterogenous hydrogel mimicking the osteochondral ECM applied to tissue regeneration. J Mater Chem B 2021;9:8646–58. https://doi.org/10.1039/D1TB00518A.
[32] Yang Z, Zhao T, Gao C, Cao F, Li H, Liao Z, et al. 3D-Bioprinted Difunctional Scaffold for In Situ Cartilage Regeneration Based on Aptamer-Directed Cell Recruitment and Growth Factor-Enhanced Cell Chondrogenesis. ACS Appl Mater Interfaces 2021;13:23369–83. https://doi.org/10.1021/acsami.1c01844.
[33] Kilian D, Ahlfeld T, Akkineni AR, Bernhardt A, Gelinsky M, Lode A. 3D Bioprinting of osteochondral tissue substitutes – in vitro-chondrogenesis in multi-layered mineralized constructs. Sci Rep 2020;10:8277. https://doi.org/10.1038/s41598-020-65050-9.
[34] Xing J, Peng X, Li A, Chen M, Ding Y, Xu X, et al. Gellan gum/alginate-based Ca-enriched acellular bilayer hydrogel with robust interface bonding for effective osteochondral repair. Carbohydr Polym 2021;270:118382. https://doi.org/10.1016/j.carbpol.2021.118382.
[35] Huang B, Li P, Chen M, Peng L, Luo X, Tian G, et al. Hydrogel composite scaffolds achieve recruitment and chondrogenesis in cartilage tissue engineering applications. J Nanobiotechnology 2022;20:25. https://doi.org/10.1186/s12951-021-01230-7.
[36] Chen Y, Chen Y, Xiong X, Cui R, Zhang G, Wang C, et al. Hybridizing gellan/alginate and thixotropic magnesium phosphate-based hydrogel scaffolds for enhanced osteochondral repair. Mater Today Bio 2022;14:100261. https://doi.org/10.1016/j.mtbio.2022.100261.
[37] Lafuente-Merchan M, Ruiz-Alonso S, García-Villén F, Gallego I, Gálvez-Martín P, Saenz-del-Burgo L, et al. Progress in 3D Bioprinting Technology for Osteochondral Regeneration. Pharmaceutics 2022;14:1578. https://doi.org/10.3390/pharmaceutics14081578.
[38] Osmałek T, Froelich A, Tasarek S. Application of gellan gum in pharmacy and medicine. Int J Pharm 2014;466:328–40. https://doi.org/10.1016/j.ijpharm.2014.03.038.
[39] Costa L, Silva-Correia J, Oliveira JM, Reis RL. Gellan Gum-Based Hydrogels for Osteochondral Repair. In: Oliveira JM, Pina S, Reis RL, San Roman J, editors. Osteochondral Tissue Eng., vol. 1058, Cham: Springer International Publishing; 2018, p. 281–304. https://doi.org/10.1007/978-3-319-76711-6_13.
[40] Chen M, Yu P, Xing J, Wang Y, Ren K, Zhou G, et al. Gellan gum modified hyaluronic acid hydrogels as viscosupplements with lubrication maintenance and enzymatic resistance. J Mater Chem B 2022;10:4479–90. https://doi.org/10.1039/D2TB00421F.
[41] Leone G, Consumi M, Pepi S, Pardini A, Bonechi C, Tamasi G, et al. Enriched Gellan Gum hydrogel as visco-supplement. Carbohydr Polym 2020;227:115347. https://doi.org/10.1016/j.carbpol.2019.115347.

[42] Akkineni AR, Elci BS, Lode A, Gelinsky M. Addition of High Acyl Gellan Gum to Low Acyl Gellan Gum Enables the Blends 3D Bioprintable. Gels 2022;8:199. https://doi.org/10.3390/gels8040199.
[43] Mouser VHM, Melchels FPW, Visser J, Dhert WJA, Gawlitta D, Malda J. Yield stress determines bioprintability of hydrogels based on gelatin-methacryloyl and gellan gum for cartilage bioprinting Biofabrication 2016, 19;8(3):035003. doi: 10.1088/1758-5090/8/3/035003
[44] Douglas TEL, Messersmith PB, Chasan S, Mikos AG, de Mulder ELW, Dickson G, et al. Enzymatic Mineralization of Hydrogels for Bone Tissue Engineering by Incorporation of Alkaline Phosphatase: Enzymatic Mineralization of Hydrogels for Bone Tissue Engineering by …. Macromol Biosci 2012;12:1077–89. https://doi.org/10.1002/mabi.201100501.
[45] Douglas TEL, Łapa A, Samal SK, Declercq HA, Schaubroeck D, Mendes AC, et al. Enzymatic, urease-mediated mineralization of gellan gum hydrogel with calcium carbonate, magnesium-enriched calcium carbonate and magnesium carbonate for bone regeneration applications: Hydrogels enzymatically mineralized with Ca/Mg-carbonate. J Tissue Eng Regen Med 2017;11:3556–66. https://doi.org/10.1002/term.2273.
[46] Zhang Y, Shu T, Wang S, Liu Z, Cheng Y, Li A, et al. The Osteoinductivity of Calcium Phosphate-Based Biomaterials: A Tight Interaction With Bone Healing. Front Bioeng Biotechnol 2022;10:911180. https://doi.org/10.3389/fbioe.2022.911180.
[47] Wang L, Huang Y, Ding K, Lai Y, Mao R, Luo F, et al. Polyphosphate enhanced biomimetic mineralization of 3D printing scaffolds for bone regeneration. Compos Part B Eng 2022;239:109989. https://doi.org/10.1016/j.compositesb.2022.109989.
[48] Lopez-Heredia MA, Łapa A, Reczyńska K, Pietryga K, Balcaen L, Mendes AC, et al. Mineralization of gellan gum hydrogels with calcium and magnesium carbonates by alternate soaking in solutions of calcium/magnesium and carbonate ion solutions. J Tissue Eng Regen Med 2018;12:1825–34. https://doi.org/10.1002/term.2675.
[49] Gkioni K, Leeuwenburgh SCG, Douglas TEL, Mikos AG, Jansen JA. Mineralization of Hydrogels for Bone Regeneration. Tissue Eng Part B Rev 2010;16:577–85. https://doi.org/10.1089/ten.teb.2010.0462.
[50] Yao J, Fang W, Guo J, Jiao D, Chen S, Ifuku S, et al. Highly Mineralized Biomimetic Polysaccharide Nanofiber Materials Using Enzymatic Mineralization. Biomacromolecules 2020;21:2176–86. https://doi.org/10.1021/acs.biomac.0c00160.
[51] Douglas T, Wlodarczyk M, Pamula E, Declercq H, de Mulder E, Bucko M, et al. Enzymatic mineralization of gellan gum hydrogel for bone tissue-engineering applications and its enhancement by polydopamine: Enzymatic mineralization of gellan gum enhanced by polydopamine functionalization. J Tissue Eng Regen Med 2014;8:906–18. https://doi.org/10.1002/term.1616.
[52] Guo Y, Du S, Quan S, Jiang F, Yang C, Li J. Effects of biophysical cues of 3D hydrogels on mesenchymal stem cells differentiation. J Cell Physiol 2021;236:2268–75. https://doi.org/10.1002/jcp.30042.
[53] Qiu Y, Xu X, Guo W, Zhao Y, Su J, Chen J. Mesoporous Hydroxyapatite Nanoparticles Mediate the Release and Bioactivity of BMP-2 for Enhanced Bone Regeneration. ACS Biomater Sci Eng 2020;6:2323–35. https://doi.org/10.1021/acsbiomaterials.9b01954.
[54] Wei S, Deng Y, Liu X, Xu A, Wang L, Luo Z, et al. Effect of surface roughness on osteogenesis in vitro and osseointegration in vivo of carbon fiber-reinforced polyetheretherketone–nanohydroxyapatite composite. Int J Nanomedicine 2015:1425. https://doi.org/10.2147/IJN.S75557.
[55] Douglas TEL, Gassling V, Declercq HA, Purcz N, Pamula E, Haugen HJ, et al. Enzymatically induced mineralization of platelet-rich fibrin. J Biomed Mater Res A 2012;100A:1335–46. https://doi.org/10.1002/jbm.a.34073.
[56] Douglas TEL, Krawczyk G, Pamula E, Declercq HA, Schaubroeck D, Bucko MM, et al. Generation of composites for bone tissue-engineering applications consisting of gellan gum hydrogels mineralized with calcium and magnesium phosphate phases by enzymatic means: Gellan gum

and calcium and magnesium phosphate composites. J Tissue Eng Regen Med 2016;10:938–54. https://doi.org/10.1002/term.1875.
[57] Flores-Merino MV, Chirasatitsin S, LoPresti C, Reilly GC, Battaglia G, Engler AJ. Nanoscopic mechanical anisotropy in hydrogel surfaces. Soft Matter 2010;6:4466. https://doi.org/10.1039/c0sm00339e.
[58] Silva-Correia J, Oliveira JM, Caridade SG, Oliveira JT, Sousa RA, Mano JF, et al. Gellan gum-based hydrogels for intervertebral disc tissue-engineering applications. J Tissue Eng Regen Med 2011;5:e97–107. https://doi.org/10.1002/term.363.
[59] Milovanovic M, Mihailowitsch L, Santhirasegaran M, Brandt V, Tiller JC. Enzyme-induced mineralization of hydrogels with amorphous calcium carbonate for fast synthesis of ultrastiff, strong and tough organic–inorganic double networks. J Mater Sci 2021;56:15299–312. https://doi.org/10.1007/s10853-021-06204-6.
[60] Nonoyama T. Robust hydrogel–bioceramics composite and its osteoconductive properties. Polym J 2020;52:709–16. https://doi.org/10.1038/s41428-020-0332-y.
[61] Axpe E, Chan D, Offeddu GS, Chang Y, Merida D, Hernandez HL, et al. A Multiscale Model for Solute Diffusion in Hydrogels. Macromolecules 2019;52:6889–97. https://doi.org/10.1021/acs.macromol.9b00753.
[62] Wu VM, Uskoković V. Is there a relationship between solubility and resorbability of different calcium phosphate phases in vitro ? Biochim Biophys Acta BBA - Gen Subj 2016;1860:2157–68. https://doi.org/10.1016/j.bbagen.2016.05.022.
[63] Pietryga K, Costa J, Pereira P, Douglas TEL, Pamula E. Promotion of bone cel growth on gellan gum hydrogels by enzymatic mineralization, Eng Biomat 2014;125:6–12.
[64] Douglas TEL, Dokupil A, Reczyńska K, Brackman G, Krok-Borkowicz M, Keppler JK, et al. Enrichment of enzymatically mineralized gellan gum hydrogels with phlorotannin-rich *Ecklonia cava* extract Seanol ® to endow antibacterial properties and promote mineralization. Biomed Mater 2016;11:045015. https://doi.org/10.1088/1748-6041/11/4/045015.
[65] Morris ER, Nishinari K, Rinaudo M. Gelation of gellan – A review. Food Hydrocoll 2012;28:373–411. https://doi.org/10.1016/j.foodhyd.2012.01.004.
[66] Sun M, Chi G, Li P, Lv S, Xu J, Xu Z, et al. Effects of Matrix Stiffness on the Morphology, Adhesion, Proliferation and Osteogenic Differentiation of Mesenchymal Stem Cells. Int J Med Sci 2018;15:257–68. https://doi.org/10.7150/ijms.21620.
[67] Zhou Y, Qiu J, Wan L, Li J. The effect of matrix stiffness on the chondrogenic differentiation of mesenchymal stem cells. J Mol Histol 2022;53:805–16. https://doi.org/10.1007/s10735-022-10094-6.
[68] Karim A, Amin AK, Hall AC. The clustering and morphology of chondrocytes in normal and mildly degenerate human femoral head cartilage studied by confocal laser scanning microscopy. J Anat 2018;232:686–98. https://doi.org/10.1111/joa.12768.
[69] Campbell SE, Ferguson VL, Hurley DC. Nanomechanical mapping of the osteochondral interface with contact resonance force microscopy and nanoindentation. Acta Biomater 2012;8:4389–96. https://doi.org/10.1016/j.actbio.2012.07.042.
[70] Di Luca A, Van Blitterswijk C, Moroni L. The osteochondral interface as a gradient tissue: From development to the fabrication of gradient scaffolds for regenerative medicine: The Osteochondral Interface as a Gradient Tissue. Birth Defects Res Part C Embryo Today Rev 2015;105:34–52. https://doi.org/10.1002/bdrc.21092.
[71] Samal SK, Dash M, Declercq HA, Gheysens T, Dendooven J, Voort PVD, et al. Enzymatic Mineralization of Silk Scaffolds: Enzymatic Mineralization of Silk Scaffolds. Macromol Biosci 2014;14:991–1003. https://doi.org/10.1002/mabi.201300513.
[72] Norris K, Kocot M, Tryba AM, Chai F, Talari A, Ashton L, et al. Marine-Inspired Enzymatic Mineralization of Dairy-Derived Whey Protein Isolate (WPI) Hydrogels for Bone Tissue Regeneration. Mar Drugs 2020;18:294. https://doi.org/10.3390/md18060294.

[73] Drobnič M, Kolar M, Verdonk P, Vannini F, Robinson D, Altschuler N, et al. Complex Osteochondral Lesions of the Talus Treated With a Novel Bi-Phasic Aragonite-based Implant. J Foot Ankle Surg 2021;60:391–5. https://doi.org/10.1053/j.jfas.2020.06.028.
[74] Goldring SR, Goldring MB. Changes in the osteochondral unit during osteoarthritis: structure, function and cartilage–bone crosstalk. Nat Rev Rheumatol 2016;12:632–44. https://doi.org/10.1038/nrrheum.2016.148.
[75] Banh L, Cheung KK, Chan MWY, Young EWK, Viswanathan S. Advances in organ-on-a-chip systems for modelling joint tissue and osteoarthritic diseases. Osteoarthritis Cartilage 2022;30:1050–61. https://doi.org/10.1016/j.joca.2022.03.012.

Appendix

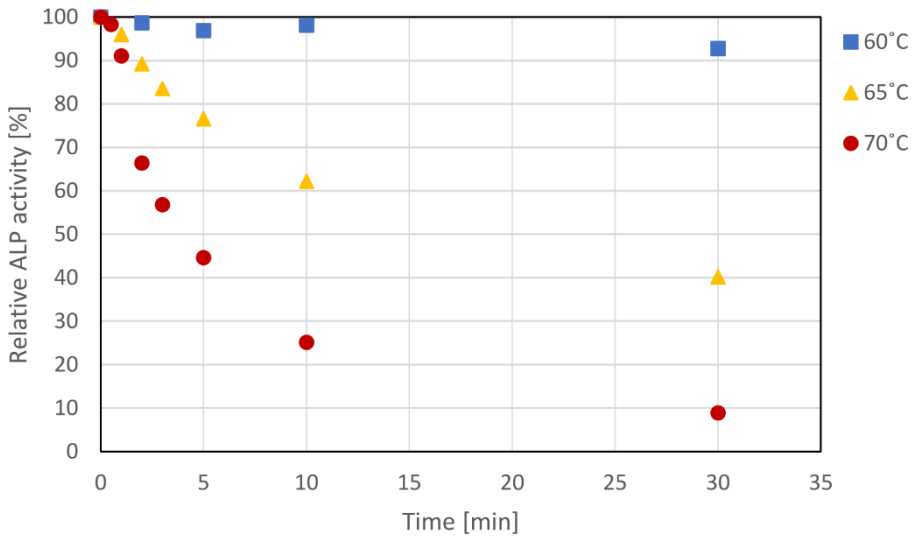

Supplementary Figure 1. ALP activity loss after incubation in high temperature conditions over time (relative to freshly made ALP solution.

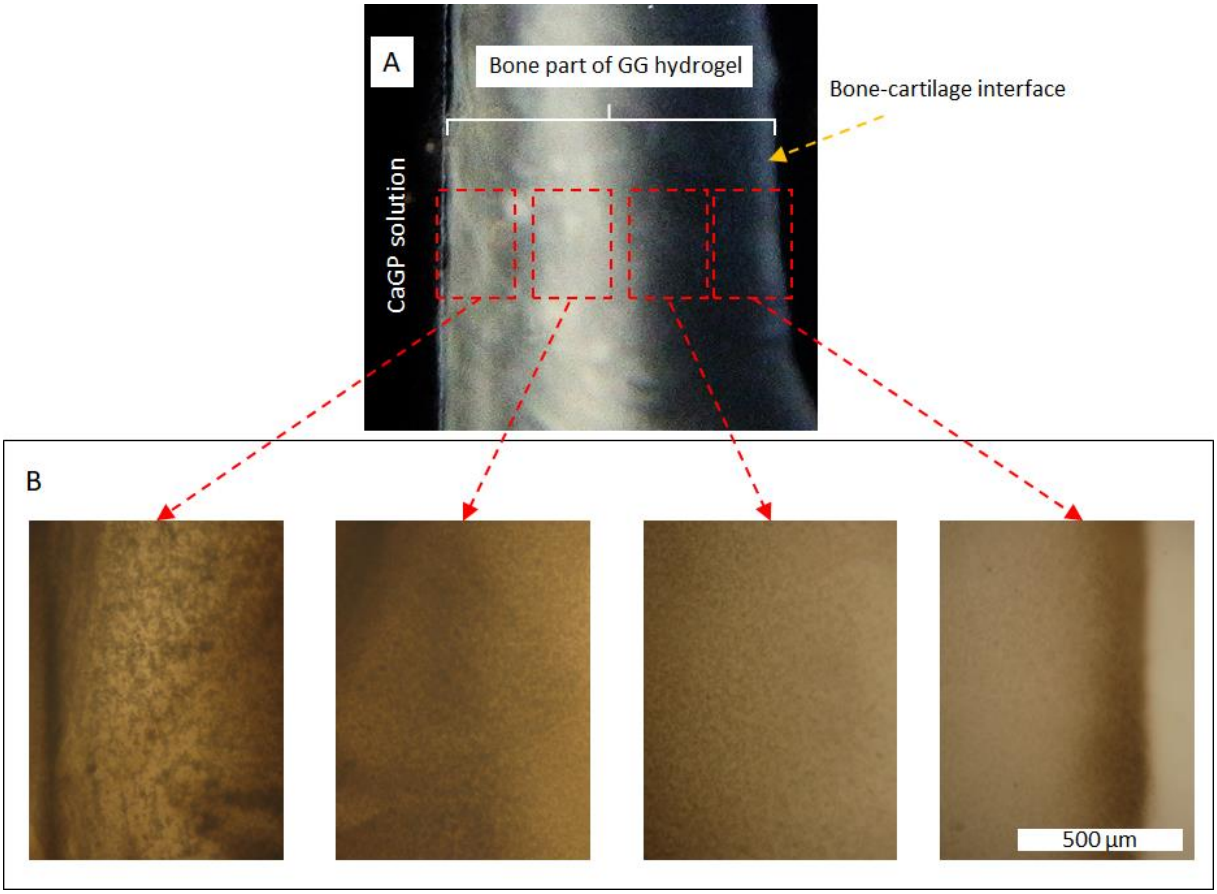

Supplementary Figure 2. Mineralization process in thin layer of hydrogel under glass slide after 3 days. Microphotography in reflected light (low magnification) and transmitted light (higher magnification) (B). Densification of mineralization process on interface is in this case also visible.